DEFORMATION OF COMPLIANT FAULT ZONES INDUCED BY NEARBY EARTHQUAKES: THEORETICAL INVESTIGATIONS IN THREE DIMENSIONS AND APPLICATIONS TO THE EAST CALIFORNIA SHEAR ZONE

A Dissertation

by

JINGQIAN KANG

Submitted to the Office of Graduate and Professional Studies of
Texas A&M University
in partial fulfillment of the requirements for the degree of

DOCTOR OF PHILOSOPHY

Chair of Committee,	Benchun Duan
Committee Members,	Frederick Chester
	Judith Chester
	Richard Gibson
	Giovanna Biscontin
Head of Department,	Rick Giardino

May 2014

Major Subject: Geophysics

ABSTRACT

Using dynamic modeling of earthquake rupture on a strike-slip fault and seismic wave propagation in a three dimensional inhomogeneous elastoplastic medium, I investigate the inelastic response of compliant fault zones to nearby earthquakes. I primarily examine the plastic strain distribution within the fault zone and the displacement field that characterizes the effects of the presence of the fault zone. I find that when the fault zone rocks are close to failure in the prestress field, plastic strain occurs along the entire fault zone near the Earth's surface and some portions of the fault zone in the extensional quadrant at depth, while the remaining portion deforms elastically. Plastic strain enhances the surface displacement of the fault zone, and the enhancement in the extensional quadrant is stronger than that in the compressive quadrant. These findings suggest that taking into account both elastic and inelastic deformation of fault zones to nearby earthquakes may improve our estimations of fault zone structure and properties from small-scale surface deformation signals. Furthermore, identifying the inelastic response of nearby fault zones to large earthquakes may allow us to place some constraints on the absolute stress level in the crust.

I also investigate how to distinguish inelastic and elastic responses of compliant fault zones to the nearby rupture. I explore in detail the range of plastic parameters that allow plastic strain to occur and examine its effect on the displacement field around compliant fault zone. I find that the sympathetic motion (i.e., consistent to long-term geologic slip) or the reduced retrograde motion (i.e., opposite to long-term geologic slip) observed in

residual displacement on fault parallel horizontal direction can be directly used to distinguish the inelastic deformation from the elastic deformation. This may help better interpret the geodetic observations in the further. In addition, I conduct models with various fault zone geometries (i.e., depth, width and shape) and rigidity reduction properties to test their effects on the displacement field. The results from elastic models suggest that to the same dynamic rupture source, the deeper and wider pre-existing nearby fault zone will result in larger residual displacement. But this only applies to fault zones with large depth extent. For shallow fault zones, residual displacement tends to keep the same magnitude or even decreases with fault zone width. While in plastic models, where plastic strain is allowed, displacement field is more complex. The magnitude of the residual displacement will be enhanced by the occurrence of plastic strain.

Then I extend the theoretical simulations of an idealized planar rupture fault system into one in a geometrically complex real fault system in the East California Shear Zone (ECSZ). I compare our simulation results of the 1992 Landers Earthquake with the geodetic observations. Responses of the Calico and Rodman compliant fault zone are better understood by taking into account of both inelastic and elastic responses of compliant fault zones to the nearby Landers rupture.

DEDICATION

To my husband, Youli Mao, for his patience and love.

To my parents, for continuously encouraging me to explore things I like.

ACKNOWLEDGEMENTS

First and foremost, I would like to thank my committee chair, Dr. Benchun Duan, for his patient and insightful guidance through my Ph.D. study. The work presented in this dissertation would not have been possible without his continuous encouragement and unreserved knowledge sharing. I also want to thank the other members of my dissertation committee, Dr. Fred Chester, Dr. Judith Chester, Dr. Gibson and Dr. Biscontin, for their guidance and support throughout the course of this research.

I would like to thank the faulty of the Geology and Geophysics department at Texas A&M University for teaching me courses. Thanks also go to my friends and colleagues and the department staff for making my time at Texas A&M University a great experience.

I also want to extend my gratitude to the National Science Foundation, Southern California Earthquake Center, Berg-Huge center which funded the works reported in this dissertation.

TABLE OF CONTENTS

Page

LIST OF FIGURES

Page

LIST OF TABLES

Page

CHAPTER I

INTRODUCTION

The main thrust of this dissertation is to use spontaneous rupture models with off-fault elastic and elastoplastic rheology to explore elastic and inelastic response of the compliant fault zones to nearby earthquakes, with applications to fault zones in the East California Shear Zone (ECSZ) and their response to the 1992 Landers earthquake. The geometry and properties of compliant fault zone may contain information of past earthquake ruptures and subsequent healing processes. In this project, we start from a theoretical point of view to study elastic and inelastic deformation around a compliant fault zone induced by a nearby earthquake in an idealized three dimensional (3D) model. We examine dependence of the surface displacement field on the fault zone structure and properties, including the width, depth extent, shape of the fault zone, rigidity reduction, internal friction and cohesion within the fault zone. These results help to improve our understanding of small-scale deformation signals around pre-existing faults due to nearby earthquakes. We also expand the above theoretical studies of dynamic rupture in an inhomogeneous 3D elastoplastic medium to a real fault system of the 1992 Landers earthquake and compare the dynamic rupture simulation results with geodetic observations. The results suggest that with both elastic and inelastic deformation, we have a more accurate view of 3D surface small-scaled strain field and compliant fault zone geometry and properties.

1.1 Background

Crustal faults are often associated with fractured and damaged rocks around the slip surface. Such compliant fault zones may result from micro-cracking, coalesce of micro-joints, grain boundary frictional sliding and other microscopic processes during dynamic rupture propagation and stress perturbation [e.g., Scholz et al, 1993; Chester et al., 1993; Chester and Chester, 1998]. Seismic trapped waves and travel time analysis are used to image compliant fault zone geometry (i.e., width and depth) and property (rigidity reduction) [e.g., Li et al., 1998; Ben-Zion and Sammis, 2003].

Recent Interferometric Synthetic Aperture Radar (InSAR) studies are also been conducted to explain the elastic response of fault zones with rigidity reduction to nearby earthquakes [e.g. Fialko et al, 2002; Fialko, 2004; Barbot et al., 2009]. Fault zones imaged by all the techniques listed above are presumably the same geologic structure. However, seismic studies reveal damaged fault zones with a width of several hundred meters [e.g., Li et al., 1998; Ben-Zion and Sammis, 2003]; While InSAR studies require fault zone widths of one to several kilometers. The depth extent of compliant fault zones is also under debate. One view is that the damaged fault zones are shallow features of top several kilometers [e.g., Ben-Zion and Sammis., 2003], while the other view is that the compliant fault zones should extend below a few kilometers, even the entire seismogenic zone [e.g., Li et al, 1998; Fialko et al., 2002; Barbot et al., 2009]. Cochran et al [2009] attempted to reconcile the differences by proposing a new model with moderate width, depth and rigidity reduction, using a Hanning taper profile. But there

are obvious misfits between their synthetic results and InSAR observations, suggesting the reconciliation isn't as good as they claimed.

Vidale and Li [2003] reported that the healing process of the Johnson Valley Fault after the 1992 Mw 7.3 Landers earthquake rupture occurred on it was interrupted by the nearby 1999 Mw 7.1 Hector Mine earthquake. Vidale and Li [2003] proposed that the dynamic stress perturbation from the nearby earthquake may have induced some microscopic processes, such as micro-cracking and/or grain-scale frictional sliding, causing damage of the fault zone rocks. This observation suggests that the response of the fault zone rocks to nearby earthquakes may not be linearly elastic.

Recent development of spontaneous rupture models allows us to simulate the inelastic deformation induced by nearby dynamic rupture [e.g., Andrews, 2005; Duan and Day, 2008; Duan, 2008a, b; Templeton and Rice, 2008; Ma, 2008]. Duan [2010] and Duan et al [2011] explored the dynamic rupture propagation in two dimensional elastoplastic medium and found that elastic and inelastic deformation could concur during dynamic rupture propagation, but along different segments of nearby fault zones. Previous InSAR studies of elastic response of the compliant fault zone to nearby static stress changes [Fialko et al., 2002; Fialko, 2004] use results from elastic models to match the data, and found that along the same fault, there are different elastic moduli along different fault segments [Barbot et al., 2009]. This may be due to negligence of the inelastic deformation occurred along some segment of the fault, leading to potential inaccuracy in estimations of the fault zone structure and rigidity reduction. Thus

dynamic rupture models in a three dimensional elastoplastic medium are needed to study deformation of fault zones due to nearby earthquakes and their structures and properties.

1.2 Problem Statement

The awareness of the importance of inelastic response in understanding the small-scaled surface deformation prompted this dissertation research. Inspired by the observational findings from Vidale and Li [2003] mentioned above, Duan et al [2011] explore the inelastic response of compliant fault zones to nearby earthquakes and the effects on the displacement field in 2D strike-slip faulting models. They find that elastic and inelastic deformation could concur during dynamic rupture propagation, but along different segments of nearby fault zone. However, the InSAR displacement field is dominated by the vertical component, which is absent in these previously published 2D models. How inelastic strain is distributed in the fault zone and how inelastic response affects the displacement field at the Earth's surface (in particular the vertical component) are important questions, which have significant implications for more accurate estimations of fault zone structure and properties from InSAR images of large earthquakes, and thus for better understanding of fault zone processes and earthquake ruptures. The two questions are addressed in this dissertation study by three dimensional elastoplastic models.

The geometry and properties of compliant fault zones may contain information of past earthquake ruptures and subsequent healing processes. In this project, I examine the dependence of the surface displacement field on the fault zone structure and properties, including the width, depth extent, shape of the fault zone, rigidity reduction and plastic

parameters of the compliant fault zone. These results help to improve our understanding of small-scale deformation signals around pre-existing faults due to nearby earthquakes.

CHAPTER II

METHODOLOGY

Numerical simulations of earthquake rupture dynamics are common in recent decades, yet it still has been difficult to test the validity of these simulation results due to few field observations constrains and no analytic solutions to compare with. The Southern California Earthquake Center/U.S. Geological Survey fund the Dynamic Earthquake Rupture Code Verification Exercise, where codes that simulate spontaneous rupture dynamics are evaluated and the results produced by these codes are compared using Web-based tools. Our group participates in this Code Verification exercise using our code EQdyna [e.g., Duan and Oglesby, 2006; Duan and Day, 2008; Harris et al., 2009, 2011; Duan, 2010a, 2010b; Duan et al., 2011], which is capable of doing various types of models.

There are a number of assumptions in a spontaneous rupture earthquake simulation. These include the geometry of the faults involved, the properties of the materials that surround and comprise the fault zone, the initial stress conditions, and the failure criterion that specifies the coseismic friction and determines whether or not points on the fault will be allowed to slip. Once we make the above assumptions and input them as initial conditions and material parameters into the numerical code, after the simulation of the earthquake as spontaneous rupture, it will give out the results such as the fault slips, ground motions, stress and strain fields, etc.

In this study, we use the Code Verification community verified finite element code EQdyna to perform the numerical simulation of 3D dynamic rupture and seismic wave propagations in inhomogeneous elastoplastic media. A slip weakening friction law [Ida., 1972; Andrews., 1976] is employed to govern the rupture propagation, in which the frictional coefficient drops from static value μ_s to dynamic value μ_d over the critical slip distance D_0 as $\mu\ (\delta) = \mu_s - (\mu_s - \mu_d)$ min $\{\delta, D_0\}/ D_0$, where δ is the slip on the fault, when shear stress on the fault reaches the yield stress. The fault edges (except at the free surface) are pinned by a high static frictional coefficient. To initiate the rupture, we prescribe a nucleation patch at the center of the fault plane, within which the rupture is forced to propagate at a fixed slow speed. Outside the nucleation patch, the rupture propagates spontaneously at faster speeds.

We use the Drucker-Prager yield criterion to describe the material failure in the medium [Drucker and Prager, 1952]. A depth dependent initial stress field has been assigned over the entire model region.

We run the dynamic simulations for a sufficient amount of time to obtain the static deformation field. The main part of the model is surrounded by a much larger buffer region. The buffer region is large enough to prevent reflections at artificial model boundaries from contaminating the simulation results.

Although the later part of this dissertation study will compare our simulation results with the static deformation field from the geodetic observation, one of the main focuses of this study is to examine the inelastic response of fault zone to the nearby rupture, in which dynamic stress perturbation from the spontaneous rupture has a significant impact

on the inelastic response of the pre-existing fault zone. This specific purpose requires dynamic rupture models, instead of static models to simulate the earthquake.

3D version of EQdyna is parallelized using a hybrid MPI/OpenMP approach [Wu et al., 2011]. Most recent development has scaled the code to run on thousands CPUs. This will allow us to perform high-resolution 3D simulations (e.g., on the order of one hundred meter element size), which may be needed for capturing fine fault zone structure and properties in this project.

At TAMU, We have two dedicated shared-memory servers in our lab in the center of Tectonophysics within the Geology and Geophysics department. One is a Dell server with 32 cores and 128 GB RAM memory. The other is a SUN UNIX server with 8 cores and 48 GB RAM memory. We have access to the TAMU supercomputing facility cluster system EOS with maximum cores of 2592 and about 9 TB RAM memories for parallel simulations. We also have access to NSF-supported XSEDE supercomputer systems, including Ranger and Lonestar at TACC, and Kraken at NICS. These computing resources are adequate for us to perform this study.

CHAPTER III

FAULT ZONE RESPONSES TO NEARBY RUPTURE OF 3D IDEALIZED MODELS IN ELASTOPLASTIC MEDIA*

3.1 Introduction

Crustal faults are often associated with fractured and damaged rocks around the slip surface. This damage results in a volume of material with increased compliance in the vicinity of the fault, thus creating a compliant fault zone. This increased compliance may result from micro-cracking, coalescence of micro-joints, grain boundary frictional sliding and other microscopic processes during dynamic rupture propagation and stress perturbation [e.g., Scholz et al, 1993; Chester et al., 1993; Chester and Chester, 1998]. Seismic trapped waves and travel time analysis have been used to image compliant fault zone geometry (e.g., width and depth) and properties (e.g. rigidity reduction) [e.g., Li et al., 1998; Ben-Zion and Sammisl, 2003; Yang et al., 2011]. InSAR images of the surface deformation field of large earthquakes have also been studied to infer compliant fault zone structure and properties, primarily based on an elastic inhomogeneous model in which anomalous displacements around a pre-existing fault are considered to be an elastic response of the compliant fault zone to nearby earthquakes [e.g., Fialko et al, 2002; Fialko, 2004; Barbot et al., 2009; Cochran et al., 2009]. Although the elastic-response model for anomalous displacements works well in many cases, there are some

* Reprinted from Tectonophysics, Vol. 612-613, J. Kang and B. Duan, "Inelastic response of compliant fault zones to nearby earthquake in three dimesions" pp. 56-62 Copyright 2014, with permission from Elsevier.

cases in which mismatch between the prediction from the elastic model and observations is obvious, such as along some displacement profiles across the Calico fault induced by 1992 Mw 7.3 Landers earthquake [Cochran et al., 2009; Barbot et al., 2009].

Vidale and Li [2003] reported that the healing process of the Johnson Valley Fault after the 1992 Mw 7.3 Landers earthquake rupture occurred on it was interrupted by the nearby 1999 Mw 7.1 Hector Mine earthquake. Vidale and Li [2003] proposed that the dynamic stress perturbation from the nearby earthquake may have induced some microscopic processes, such as micro-cracking and/or grain-scale frictional sliding, causing damage of the fault zone rocks. This observation suggests that the response of the fault zone rocks to nearby earthquakes may not be linearly elastic.

The inelastic response of compliant fault zones to nearby earthquakes and the effects on the displacement field in 2D strike-slip faulting models have been studied by Duan and co-workers [Duan, 2010a; Duan et al, 2011]. They find that the inelastic response of a compliant fault zone can occur in the extensional quadrant of the nearby rupture when the fault zone rocks are initially close to failure, and that the inelastic response may result in an opposite sense of the horizontal motion across the fault zone with respect to that due to an elastic response in these 2D models. They also point out that neglecting the inelastic response of a compliant fault zone may cause inaccurate estimates of the fault zone structure and properties from observed InSAR displacement fields. However, the InSAR displacement field is dominated by the vertical component, which is absent in these previously published 2D models. How inelastic strain is distributed in the fault zone and how inelastic response affects the displacement field at the Earth's surface (in

particular the vertical component) are important questions, which have significant implications for more accurate estimations of fault zone structure and properties from InSAR images of large earthquakes, and thus for better understanding of fault zone processes and earthquake ruptures. We address the two questions in this three dimensional study.

We remark that compliant fault zones in nature may respond to nearby earthquakes elastically in many cases, as proposed in previous InSAR studies [e.g., Fialko et al., 2002; Cochran et al., 2009; Barbot et al., 2009]. However, this study is to explore effects of inelastic response due to dynamic stress perturbations on the displacement field as suggested by Vidale and Li [2003], using dynamic rupture models. Thus, in setting up models, we choose fault zone parameters that are prone to inelastic response. We do not attempt to compare with data in this study, which will be a part of future work.

3.2 Methodology

We use a community verified finite element code EQdyna [e.g., Duan and Oglesby, 2006; Duan and Day, 2008; Harris et al., 2009, 2011; Duan, 2010a, 2010b; Duan et al., 2011] to perform the numerical simulation of 3D dynamic rupture and seismic wave propagations in inhomogeneous elastoplastic media in this study. A slip weakening friction law [Ida., 1972; Andrews., 1976] is employed to govern the rupture propagation, in which the frictional coefficient drops from static value μ_s to dynamic value μ_d over the critical slip distance D_0 as $\mu(\delta) = \mu_s - (\mu_s - \mu_d) \min\{\delta, D_0\}/D_0$, where δ is the slip on the fault, when shear stress on the fault reaches the yield stress. We choose values for D_0 of 0.4 m, μ_s and μ_d of 0.6 and 0.3, respectively. The fault ends are pinned

by a high static frictional coefficient. The dynamic frictional coefficient is linearly tapered from 0.3 to 0.6 at the top and bottom parts of the seismogenic depth to reduce the dynamic stress drop gradually. To initiate the rupture, we prescribe a nucleation patch at the center of the fault plane, within which the rupture is forced to propagate at a fixed slow speed. Outside the nucleation patch, the rupture propagates spontaneously at faster speeds (Figure 3.1).

We use the Drucker-Prager yield criteria to describe the material failure in the medium. This criterion [Drucker and Prager, 1952] requires that at a point in the medium, the stress condition satisfies:

$$\sqrt{0.5 s_{ij} s_{ij}} \leq - (\sigma_{kk}/3) \sin\varphi + c \cos\varphi \qquad (1)$$

Where s_{ij} is the deviatoric stress, $\sigma_{kk}$is the first invariant of the stress tensor, summation over repeated indices is assumed, c is cohesion and φ is the internal frictional angle. The left side of the equation is the square root of the second invariant of the deviatoric stress tensor, which is regarded as a measure of the shear stress in the 3D stress state. The right side of the equation is the yield stress. When the criterion is violated, stresses are adjusted to the yield level. The increments of plastic strain components at one time step $\delta\varepsilon_{ij}^{p}$ are calculated from the adjustment to the corresponding stress component and shear modulus [e.g., Duan and Day, 2008]. Following Ma [2008] and Ma and Andrews [2010], we use a scalar quantity η(t) to evaluate the accumulated inelastic strain due to yielding at time t with $\eta(0) = 0$ as follows:

$$\eta(t) = \eta(t - \Delta t) + \delta\eta\Delta t \ , \qquad \delta\eta = \sqrt{0.5(\delta\varepsilon_{ij}^{p} - \delta\varepsilon_{kk}^{p}/3)(\delta\varepsilon_{ij}^{p} - \delta\varepsilon_{kk}^{p}/3)} \ . \qquad (2)$$

A depth dependent initial stress field has been assigned over the entire model region. In our coordinate system, the x axis is parallel to the fault plane, the y axis is perpendicular to the fault plane, and the z axis is vertical (Fig 1). For normal stress, we prescribe σ_{zz} as the effective lithostatic stress σ_{eff} (i.e., - (ρ - ρ_w)gz = - (16.37 Mpa/Km)z, where ρ and ρ_w are the density of rock and of water, respectively, assuming water level at the free surface, g is the gravitational constant and z is the depth). The sign of stresses has followed the convention in continuum mechanics (i.e., compression is negative); while $\sigma_{xx} = 1.25\,\sigma_{eff}$, $\sigma_{yy} = 0.75\,\sigma_{eff}$. For shear stress, we assume σ_{xy} = - $0.433\sigma_{eff}$, $\sigma_{xz}=\sigma_{yz}=0$. This stress state implies the fault plane is optimal in the initial stress field.

We run the dynamic simulations for a sufficient amount of time (i.e., 30 seconds) to obtain the static deformation field. The main part of the model is surrounded by a much larger buffer region. The buffer region (not shown) is large enough to prevent reflections at artificial model boundaries from contaminating the simulation results. An elements size of 100 m in the main model region is used.

3.3 Models and Results

We consider a vertical right-lateral strike-slip faulting regime in a half space in this study (Figure 3.1). The fault that ruptures is 20 km long along strike and 15 km wide along dip. We do not include a compliant fault zone surrounding the ruptured fault in the models, as our objective in this study is to investigate the response of a compliant fault zone that is some distance away from the ruptured fault. We simulate a pair of models, a target model and a reference model, to extract signals in the final displacement field that

are associated with a pre-existing compliant fault zone. In the target model, the ruptured fault is embedded in an inhomogeneous medium, with a compliant fault zone parallel to the ruptured fault plane whose center is 6 km away from the ruptured fault (Figure 3.1a). The compliant fault zone is 1.2 km wide and extends to 3 km depth from the Earth's surface. We do not explicitly include a fault within this compliant zone in the model, as we do not examine rupture triggering in this study.

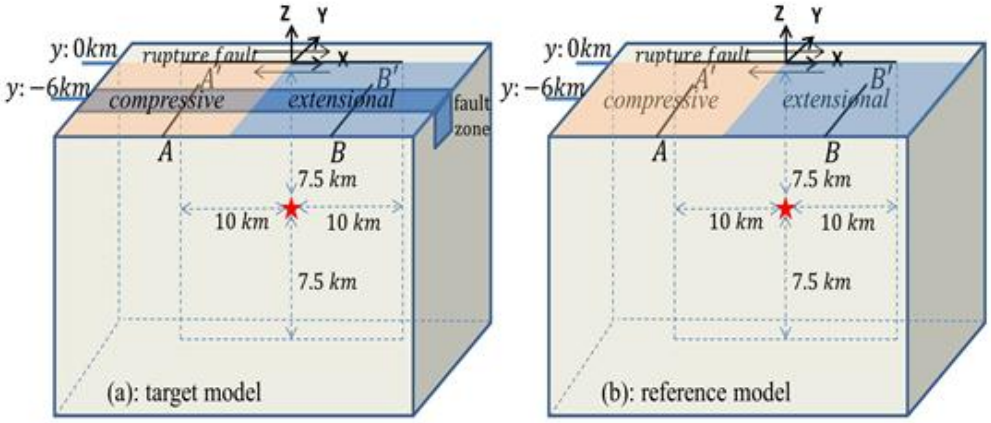

Figure 3. 1 (a) The target model in this study. The fault that ruptures in the model is 20 km long along strike and 15 km wide along dip. Rupture nucleates at the center of the fault plane, while the epicenter is the origin of the coordinate system. The compliant fault zone is 1.2 km wide and vertically extends to 3 km depth from the Earth's surface and its center is 6 km away from the rupture fault. Seismic velocity within the compliant fault zone has a 40% reduction compared with that in the host rocks. AA' and BB' are two profiles shown in the Figure found on page 20. As marked in the figure, AA' is in the compressive quadrant where it experiences compressive change in the mean stress; while BB' is in the extensional quadrant where it experiences extensional change in the mean stress. (b) The reference model. The compliant fault zone is excluded but otherwise it is the same as the target model.

The material properties of the host rock are typical of crustal rocks, i.e., the P wave and S wave velocities are 6000 m/s and 3464 m/s, respectively, and density is 2670 kg/m^3. Within the compliant fault zone, seismic velocities are reduced by 40%, while the density is the same. For plastic parameters, i.e., internal friction coefficient tanφ and cohesion c, we choose 0.75 and 10 MPa for the host rocks, and 0.5 and 3.5 MPa for the compliant fault zone rocks, respectively. We remark that these values of the parameters are within the range reported in the literature [e.g., Handin, 1969; Jaeger and Cook, 1976]. We also remark that the internal friction coefficient of a material is not the same as its external (sliding) friction coefficient in general [Handin, 1969]. The smaller values for the compliant fault zone rocks are chosen based on the following two considerations. First, field observations show that fault zone rocks are associated with higher crack/fracture densities compared with host rocks [e.g., Scholz et al., 1993; Chester et al., 1993; Chester and Chester, 1998], which suggests that fault zone rocks are weaker than host rocks. Second, the objective of this study is to investigate effects of inelastic response of compliant fault zones on the displacement field. Thus, the small values are chosen to allow obvious inelastic deformation to occur within the compliant fault zone after a large set of parameter tests. These tests (not shown) suggest that the compliant fault zone may respond to nearby earthquakes inelastically, only when the fault zone rocks are close to failure in the prestress field.

In the reference model, we exclude the compliant fault zone, but otherwise the reference model is the same as the target model (Figure 3.1b). By subtracting the displacement of the reference model from that of the target model, we obtain a residual

displacement, which characterizes the effect of the presence of the compliant fault zone on the displacement field.

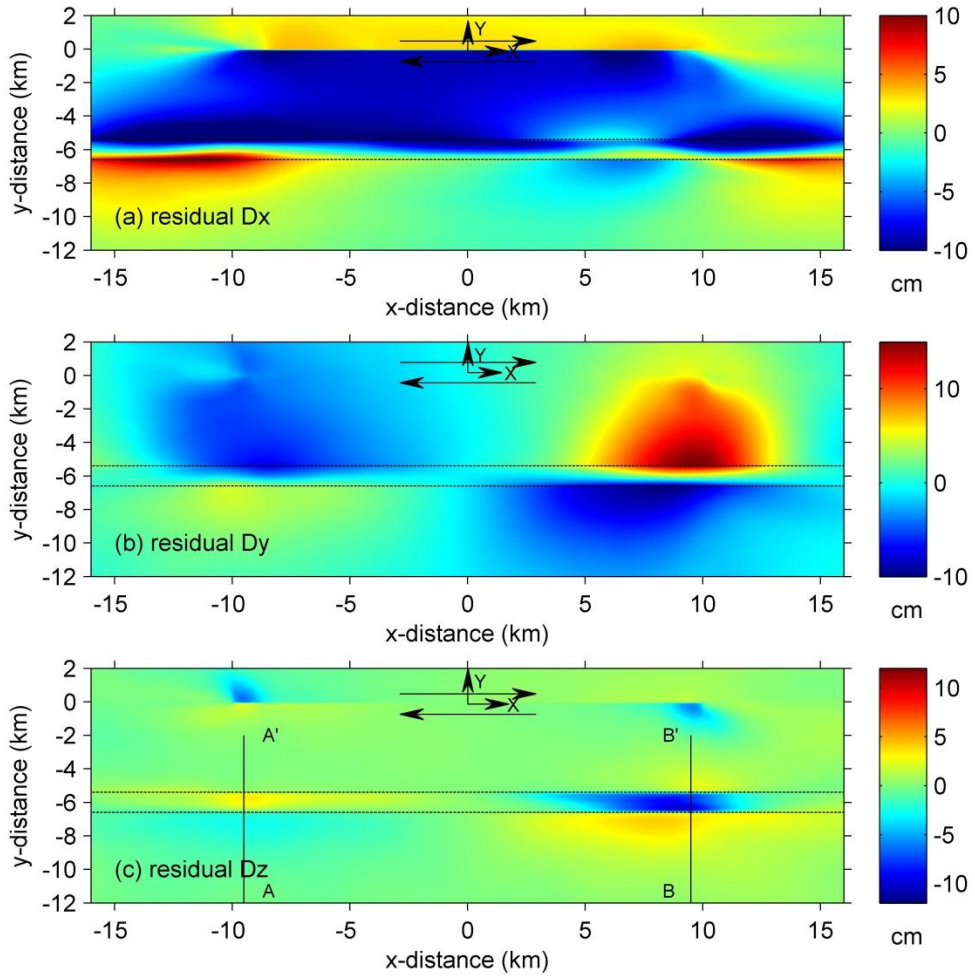

Figure 3. 2 Residual displacements (see text for definition) on the Earth's surface induced by an earthquake on a right-lateral strike-slip fault in a 3D elastoplastic inhomogeneous media with a compliant fault zone. (a) fault-parallel (x) component Dx, (b) fault-normal (y) component Dy, (c) vertical (z) component Dz. Black arrows denote the right-lateral motion on the fault. Black dash lines delimit the fault zone. AA'(x=-9.5 km) and BB' (x=9.5 km) are two profiles shown in the figure found on page 20.

Figure 3.2 shows the surface residual displacement field from the models. The deformation signals across the compliant fault zone in the two horizontal components (a and b) exhibit features similar to those reported from 2D models [Duan, 2010a; Duan et al., 2011]. Within the extensional quadrant (see Figure 3.1 for location) of the rupture, a portion of the fault zone (i.e., from ~4 km to ~9 km along x) experiences sympathetic fault-parallel motion (consistent with long-term geologic slip, i.e., right-lateral in the model) across the fault zone, while the rest of the fault zone experiences retrograde fault-parallel motion (opposite to the long-term geologic slip, i.e., left-lateral in the model). We remark that the sympathetic fault-parallel motion in this model would be less obvious, or even disappear if the fault zone were stronger (i.e., with higher internal friction coefficient and/or higher cohesion). However, as long as plastic yielding occurs there (see discussion below), retrograde motion will be reduced compared to the case of elastic deformation there. Fault-normal dilation across the compliant fault zone occurs in the extensional quadrant of the rupture, while fault-normal shortening in the compressive quadrant (see Figure 3.1 for location). Notice that the magnitude of dilatation is larger than that of shortening in the model.

The vertical component of the residual displacement at the Earth's surface (Figure 3.2c), which is absent in 2D models [Duan, 2010a; Duan et al, 2011], shows enhanced subsidence of the fault zone in the extensional quadrant of the rupture (i.e., around the BB' profile), and enhanced uplift in the compressive quadrant (i.e., around the AA' profile), due to the presence of the compliant fault zone. In particular, the enhancement

in subsidence is stronger than that in uplift. The result also suggests that subsidence and uplift of the host rock near the compliant fault zone in the extensional and compressive quadrants, respectively, are reduced by the presence of the compliant fault zone, and the reduction in subsidence is more significant than that in uplift.

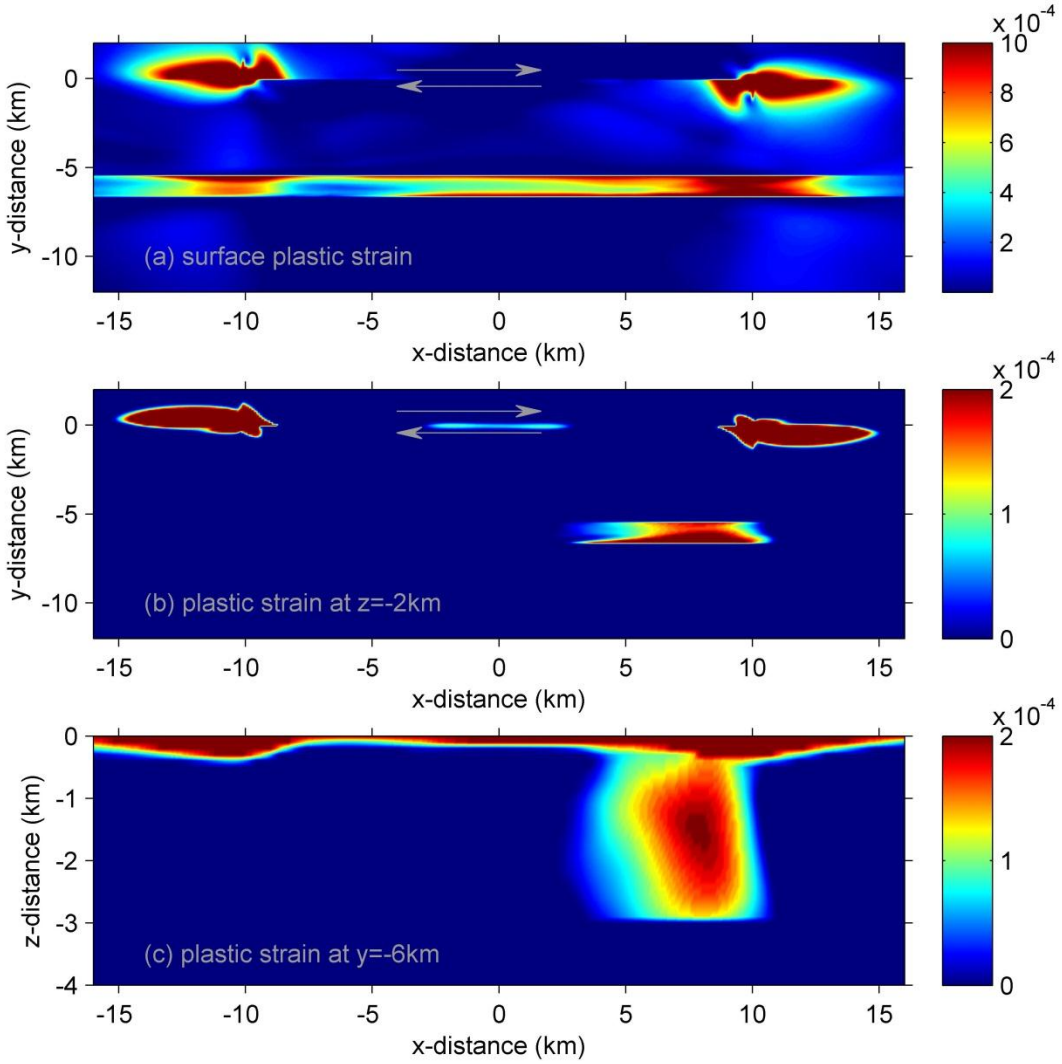

Figure 3. 3 Plastic strain distribution on (a) the Earth's surface, (b) a horizontal plane at 2km depth (z=-2km), and (c) a vertical plane at the middle of the fault zone (y=-6km). Notice that the color scale for (a) is different from those for (b) and (c).

The above contrasts in the deformation field around the compliant fault zone between the extensional and compressive quadrants of the rupture may be attributed to the difference in plastic strain distribution along the compliant fault zone in the target model (Figure 3.3). Because of small confining pressure near the Earth's surface, plastic yielding occurs along the entire fault zone (i.e., in both extensional and compressive quadrants) at very shallow depth (Figure 3.3a and 3.3c), though the plastic strain magnitude in the extensional quadrant is larger than that in the compressive quadrant. Below several hundred meters from the Earth's surface, plastic yielding only occurs along a portion of the compliant fault zone within the extensional quadrant (Figure 3.3b and 3.3c). Therefore, below several hundred meters from the Earth's surface, different portions of the compliant fault zone respond to the nearby rupture differently, i.e., elastic response within the compressive quadrant and inelastic response within some portion of the extensional quadrant. The difference in response at depth results in the difference in the deformation signals discussed above. We remark that plastic strain induced by the nearby rupture is a result of dynamic stress perturbations [e.g. Duan, 2010a; Duan et al, 2011], which vary spatially. With large confining pressure at depth, plastic strain only occurs in the extensional quadrant, where rocks experience tensile changes in mean stress, which weaken rocks. On the other hand, compressive changes in mean stress within the compressive quadrant strengthen rocks and inhibit plastic yielding.

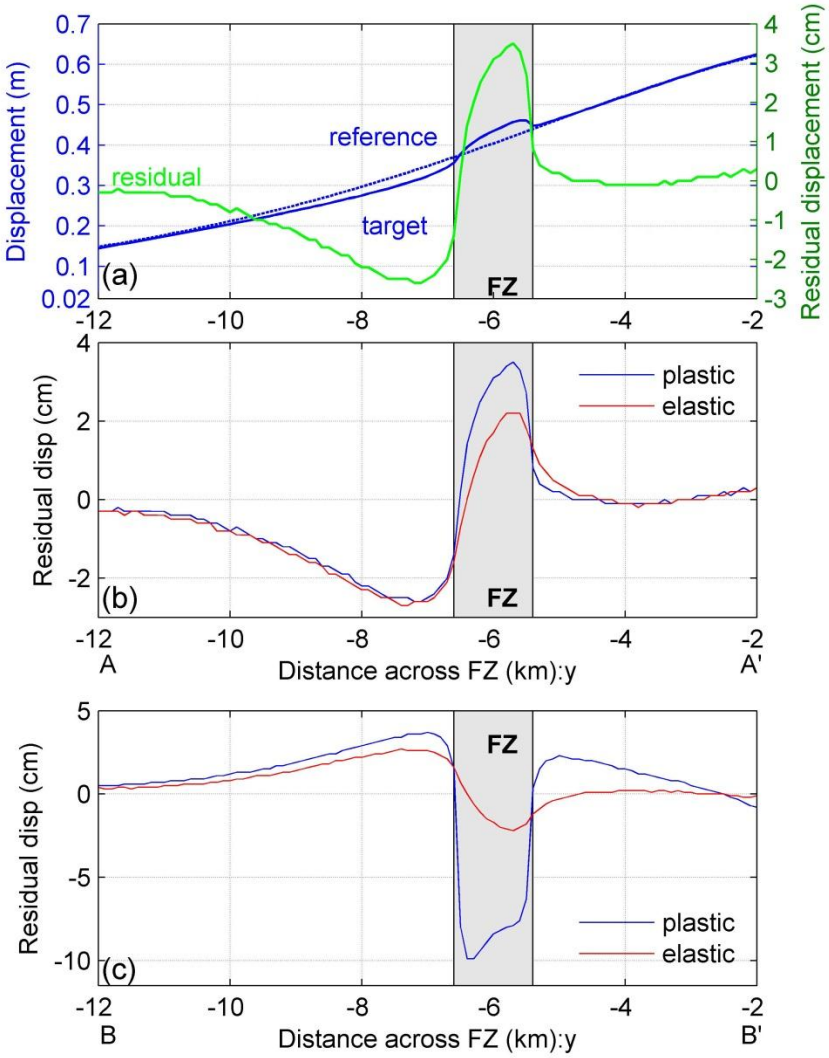

Figure 3. 4 (a) Vertical displacements along profile AA' (see Figure 3.1 and Figure 3.2c for location). Residual displacement (green curve, in centimeter on the right axis) is calculated by subtracting static displacement (in meter on the left axis) of a reference model (dash blue) from that of the target model (solid blue). Target model and reference model (dash blue) from that of the target model (solid blue). Target model and reference model are defined as in Figure 3.1 (a) and (b), respectively. (b) Vertical residual displacements along profile AA' from the plastic and elastic models, respectively. (c) Vertical residual displacements along profile BB' (see Figure 3.1 and Figure 3.2c for location) from the plastic and elastic models, respectively. Shaded bands correspond to the width of the fault zone.

To illustrate the effects of inelastic response of the compliant fault zone on the displacement field, we also run another pair of a target model and a reference model. The only change in this pair of models, with respect to the above pair of models, is that a much higher value of cohesion (e.g., 10000 MPa) is assigned to the entire model region so that no off-fault yielding will occur in this pair of models. We refer this pair of models as the elastic models, and the previous pair of models as the plastic models for convenience hereafter. In Figure 3.4, we show the vertical component of the residual displacement along two profiles AA' (in the compressive quadrant) and BB' (in the extensional quadrant, see Figure 3.1 and Figure 3.2c for location) to quantify effects of inelastic response. Figure 3.4 (a) illustrates how the residual displacement is obtained from final displacements of the target model and the reference model discussed earlier along the profile AA' in the plastic models. Figure 3.4(b) and 3.4(c) compare the residual vertical displacement from the plastic models (i.e., Figure 3.2c) and the elastic models along the profiles AA' and BB', respectively. It appears that inelastic response of the compliant fault zone enhance surface vertical displacement of the compliant fault zone significantly, in particular subsidence in the extensional quadrant (e.g., BB'). Shallow plastic yielding in the compressive quadrant (Figure 3.3) enhances uplift about 1.5 cm along AA' (Figure 3.4b), while more extensive yielding along the entire depth range of the fault zone in the extensional quadrant (Figure 3.3) enhances subsidence as large as ~7 cm along BB' (Figure 3.4c). Also notice that although shallow yielding within the fault zone along AA' does not have obvious effects on reduced uplift of the surrounding host rock (i.e., overlap of the two curves outside of the fault zone in Figure

3.4b), extensive yielding within the fault zone at depth along BB' further reduces subsidence of the surrounding host rock (i.e., larger positive values outside of the compliant fault zone from the plastic models than that from the elastic models in Figure 3.4c).

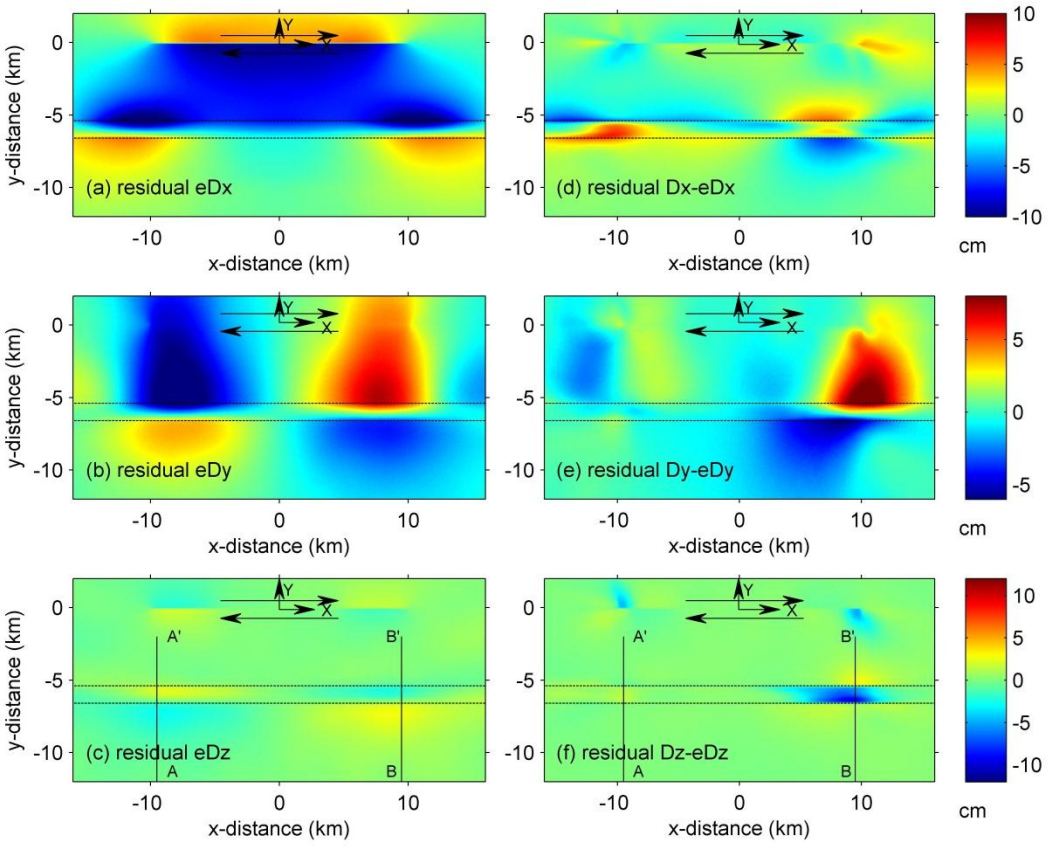

Figure 3. 5 (a), (b) and (c) are the residual displacements at the Earth's surface of the elastic models, which are marked as eDx, eDy and eDz, respectively (see text for details). (d), (e) and (f) are the differences in residual displacements between the plastic models and the elastic models. (a) and (d): fault-parallel component, (b) and (e): fault-normal component, (c) and (f): vertical component. Other symbols are same as in Figure 3. 2.

The three components of the residual surface displacement from the elastic models are shown in Figure 3.5(a)-(c), which can be compared with those in Figure 3.2. A striking contrast between the two sets of models in the fault-parallel component (Figure 3.2a and 3.5a) is the opposite sense of motion across the fault zone in the extensional quadrant. In the fault-normal horizontal component and the vertical component, deformation in the compressive and extensional quadrants is anti-symmetric, i.e., opposite sense of motion (extension versus compression, uplift versus subsidence) and similar magnitude, in the elastic models, while the magnitude of deformation is much larger in the extensional quadrant than that in the compressive quadrant in the plastic models. This may be more clearly seen from Figure 3.5(d)-(f), which shows the difference in corresponding residual displacement components between the two sets of models. The difference is significant and striking in the extensional quadrant, while it is minor to moderate in the compressive quadrant. Extensive inelastic response within the fault zone in the extensional quadrant (Figure 3.3) is the key factor that causes the contrast in the deformation signal along the compliant fault zone between the two quadrants in the plastic models.

3.4 Discussions

Previous 2D studies [Duan, 2010a; Duan et al, 2011] show that the inelastic response of a compliant fault zone occurs only in the extensional quadrant of a nearby rupture, when the compliant fault zone rocks are close to failure in the initial stress field. The condition for inelastic response to occur holds in 3D models, i.e., the fault zone rocks need to be close to failure in the prestress field. Therefore, the inelastic response of a

fault zone may be used to infer stress level within the fault zone, as the fault zone rock strength may be measured in the laboratory. However, 3D models here show that inelastic response can also occur in the compressive quadrant of the rupture at shallow depth because of small confining pressure. This appears to be a 3D effect that is associated with depth-dependent confining pressure. The shallow plastic yielding in the compressive quadrant enhances surface displacement (e.g., uplift), though it is less significant than that in the extensional quadrant. This enhanced surface displacement may be mapped into larger reduction of rigidity of the fault zone rock and/or a wider or deeper fault zone, if an elastic response is assumed. More significant enhancement in surface displacement (e.g., subsidence) by extensive inelastic response within the extensional quadrant may result in a poor match between observations and predictions from an elastic inhomogeneous model (e.g., across the Calico fault due to the 1992 Mw 7.3 Landers earthquake [Figure 6a in Barbot et al., 2009; Figure 4B in Cochran et al., 2009]). We speculate that extensive inelastic deformation of the Calico fault zone may have occurred in the extensional quadrant of the Landers rupture. We will investigate this in future work.

Our parameter tests show that the magnitude of the residual displacement of the compliant fault zone in the plastic models, in particular within the extensional quadrant, depends on the inelastic strain distribution and magnitude within the fault zone, which are in turn controlled by the prestress condition, fault zone strength (i.e., plastic parameters), and dynamic stress perturbations. However, the pattern in plastic strain distribution and the effects of inelastic response on the residual displacement discussed

above hold. We notice that the magnitude of the residual displacement along BB' in our plastic models above may be greater than those observed in the East California Shear Zone (ECSZ) [e.g., Fialko et al., 2002; Cochran et al., 2009; Barbot et al., 2009]. However, the fault zone in our model is only 6 km away from the ruptured fault, while the distance between the Calico fault and the Lander rupture is about 10 km. These differences suggest the results from our model in this study may not be directly applicable to ECSZ. Using InSAR displacement observations in ECSZ to constrain our elastoplastic inhomogeneous models will be part of our future work.

Our results suggest it is possible to distinguish between elastic and inelastic response from the residual displacement field, in particular if one can separate the horizontal and vertical residual displacements from the line-of-sight displacement in InSAR images [e.g., Fialko et al., 2002]. As reported in 2D studies [Duan, 2010a; Duan et al., 2011] and shown in Figure 3. 2a in this 3D study, inelastic response of a compliant fault zone with a certain level of plastic deformation can result in sympathetic motion across a strike-slip fault zone exhibited in the fault-parallel horizontal displacement, while elastic response results in retrograde motion [e.g., Fialko et al., 2002]. This contrast can be directly used to distinguish the two types of response. As discussed earlier, if plastic strain within a compliant fault zone is weak, sympathetic motion may be not obvious or even disappear. In this case, one may still distinguish inelastic response from elastic response by examining the fault-parallel horizontal displacement in the conjunction with the vertical displacement: compared with purely elastic response, weak inelastic response causes reduced retrograde fault-parallel motion while enhanced

vertical motion (e.g., comparing Figure 3.2a with Figure 3.5a and Figure 3.2c with Figure 3.5c around BB'). Therefore, we may distinguish the two types of response solely from the residual displacement field without knowledge of material properties.

Hearn and Fialko [2009] studied deformation signals associated with co-seismic softening of a compliant fault zone, and they found that coseismic softening of a compliant fault zone may cause centimeters of coseismic subsidence of both the complaint zone and the surrounding region, due to gravitational contraction. In our models, we do not allow coseismic softening to occur, i.e., there is no change in rock properties, including rigidity and strength, during the coseismic process. The small scale deformation signals in our models are exclusively caused by the presence of a pre-existing compliant zone with its elastic or inelastic response to a nearby rupture. Nevertheless, gravity is included in our models.

We do not include a compliant zone surrounding the ruptured fault in the above models. This is to avoid complexity in setting up model parameters [Duan, 2010a]. Yielding in a weaker compliant fault zone surrounding a rupturing fault will compete with spontaneous rupture propagation on the fault, and may not allow spontaneous rupture on the fault to sustain. As our objective in this study is to examine inelastic response of a compliant fault zone some distance away from a rupturing fault, whether or not a compliant zone surrounding the rupturing fault is included in models does not affect the above conclusions.

Fault zone structure is significantly simplified in the models of this study. Field observations show that fracture density decreases away from the fault core [e.g., Chester

et al., 1993; Chester and Chester, 1998], which suggests that rigidity reduction and cohesion within the fault zone are not uniform. Rather, they may change continuously within the fault zone. In addition, the dependence of inelastic response (e.g., plastic yielding) on fault zone structure and properties needs a parameter-space study. We will address these issues in future studies.

3.5 Conclusion

Inelastic response of a compliant fault zone to nearby earthquakes requires dynamic analyses. Using spontaneous rupture models in a 3D half space, we investigate the distribution of plastic strain within a fault zone and its effects on surface displacement fields around the fault zone. We find that when the fault zone rocks are close to failure in the prestress field, plastic strain occurs along the entire fault zone near the Earth's surface and along some portions of the fault zone in the extensional quadrant at depth, while the remaining part of fault zone deform elastically. Plastic strain within the fault zone enhances the surface displacement of the fault zone, and the enhancement in the extensional quadrant is significantly larger in magnitude than that in the compressive quadrant. The enhancement by inelastic response of the fault zone may be mapped into inaccurate estimates of the fault zone structure and/or properties from observed displacement fields if elastic response is assumed, in particular in the extensional quadrant of an earthquake rupture. By resolving the horizontal and vertical surface displacement from the line-of-sight displacement in InSAR images, one can distinguish inelastic response from elastic response of a compliant fault zone. Compared with purely elastic response, inelastic response of a compliant fault zone results in sympathetic

motion (or reduced retrograde motion) in the fault-parallel horizontal displacement while enhanced vertical displacement in a strike-slip fault system.

CHAPTER IV

ELASTIC AND INELASTIC RESPONSES OF FAULT ZONE TO NEARBY RUPTURE: PARAMETER RANGE TESTS

4.1 Introduction

Field and laboratory studies indicate that compliant fault zones, within which rock rigidity is reduced compared with that of surrounding host rocks, can result from micro-fracturing and other types of damage during dynamic rupture propagation and stress perturbation [e.g., Lockner et al, 1992; Scholz et al, 1993; Chester et al., 1993; Chester and Chester, 1998]. Compliant fault zones studies are of considerable interests because they contain information about the previous ruptures and the subsequent healing processes over earthquake cycles [e.g., Scholz et al, 1993; Fialko et al, 2002; Vidale and Li, 2003]. The geometry (i.e. fault zone width, depth, and shape) and properties (i.e., rigidity reduction) of such fault zones are critical to understand the fault zone mechanics. However, estimations of these fault zone parameters, in particular fault zone width and depth, can be significant different from different studies.

Field studies on the micro-fracture features of fault damaged rocks reveal that San Gabriel and Punchbowl faults are of 100~200 m wide at the Earth's surface [Chester et al., 1993; Chester and Chester, 1998; Ben-Zion and Sammis, 2003]. The fault zone of San Andreas Fault (SAF) at Parkfield is studied by the seismic trapped waves analysis [Li et al., 2006; Li and Malin, 2008]. They propose 30-40 m wide fault-core embedded in a 100-200 m wide jacket, which is confirmed by the San Andreas Fault Observatory

at Depth (SAFOD) drilling and logging [Hickman et al, 2005; Ellsworth and Malin, 2006]. Li et al also suggests the damage zone of SAF at Parkfield has an at least 7 km depth extent and the "V" shape (i.e., fault zone width decreases with depth). Interferometric Synthetic Aperture Radar (InSAR) images of the surface deformation field of large earthquakes have also been studied to explore compliant fault zone geometry and properties [e.g., Fialko et al, 2002; Fialko, 2004; Barbot et al., 2009; Cochran et al., 2009]. They consider the centimeter-scaled anomalous displacements around a pre-existing fault observed in the InSAR images of recent large earthquakes to be an elastic response of compliant fault zone to nearby dynamic ruptures in the elastic inhomogeneous models. The InSAR study of Barbot et al [2009] indicates the Calico fault zone in Mojave dessert is 2 km wide and has a uniform shallow depth extent of 4 km. Seismic travel time analysis by Yang et al [2011] suggests Calico fault zone is 1.3 km wide and extends to 3 km in depth. Cochran et al [2009] combine the seismic travel time analysis, fault zone trapped waves data and the geodetic observations of Calico fault zone. By fitting all the observations, they propose a ~1.5 km wide, 12 km deep and "V" shape fault zone, using horizontal and vertical taper profiles for rigidity reduction property. In studies of compliant fault zone responses to nearby ruptures, it is still unclear how the displacement associated with a fault zone depends on its geometry (e.g., the fault zone width, depth and shape) and properties (e.g., rigidity reduction). One goal of this study is to fill the gap. From a forward modeling perspective, we conduct many sets of numerical experiments. By comparing the results from different sets of experiments, we isolate the effect of fault zone parameters on the displacement field in

the elastic inhomogeneous model. The results may provide some baselines to interpret geodetic observations for future studies.

The healing process of the Johnson Valley Fault after the 1992 Mw 7.3 Landers earthquake was interrupted by the nearby 1999 Mw 7.1 Hector Mine earthquake, suggesting that fault zone responses to nearby dynamic ruptures can be beyond linear elasticity [Vidale and Li, 2003]. Vidale and Li [2003] proposed that the dynamic stress perturbation from the nearby earthquake may have induced some microscopic processes, such as micro-cracking and/or grain-scale frictional sliding, causing damage of the Johnson Valley fault zone rocks.

The inelastic response of compliant fault zones to nearby earthquakes and its effects on the displacement field in strike-slip faulting models have been studied by Duan and co-workers in both 2D and 3D using the elastoplastic inhomogeneous model [Duan, 2010a; Duan et al, 2011; Kang and Duan, 2014].They find that in 2D models, when initial shear stress is set to be close to the material strength, plastic strain can be observed within the fault zone of the extensional quadrant which experiences the extensional mean stress change, resulting in sympathetic motion in the horizontal residual displacement field; while the rest of fault zone responses to the nearby earthquake elastically and displays retrograde motion in residual displacement field. In their recent 3D study [Kang and Duan, 2014], they find that plastic strain can occur along the entire fault zone near the Earth's surface and some portions of the fault zone in the extensional quadrant at depth, while the remaining portion deforms elastically. Plastic strain enhances the surface displacement of the fault zone, and the enhancement

in the extensional quadrant is stronger than that in the compressive quadrant. However, the previous 3D work focuses on the distribution of plastic strain and its effects on the displacement field with limited case studies. Therefore, the other goal of this study is to examine how plastic parameters (i.e., internal friction coefficient tanφ and cohesion c) affect inelastic response of compliant fault zones, and how the displacement field varies with fault zone geometry and properties in the elastoplastic inhomogeneous model. We remark that we do not attempt to compare with data in this study, which will be a part of future work.

4.2 Methods and Models

In this study, we consider a vertical right-lateral strike-slip faulting regime in a half space (Figure 4.1). The fault that ruptures is 20 km long along strike and 15 km wide along dip. In the target model, the ruptured fault is embedded in an inhomogeneous medium, with a compliant fault zone parallel to the ruptured fault plane whose center is 6 km away from the ruptured fault. The compliant fault zone in Figure 4.1a is "U"-shape (i.e., fault zone has a uniform width along depth).

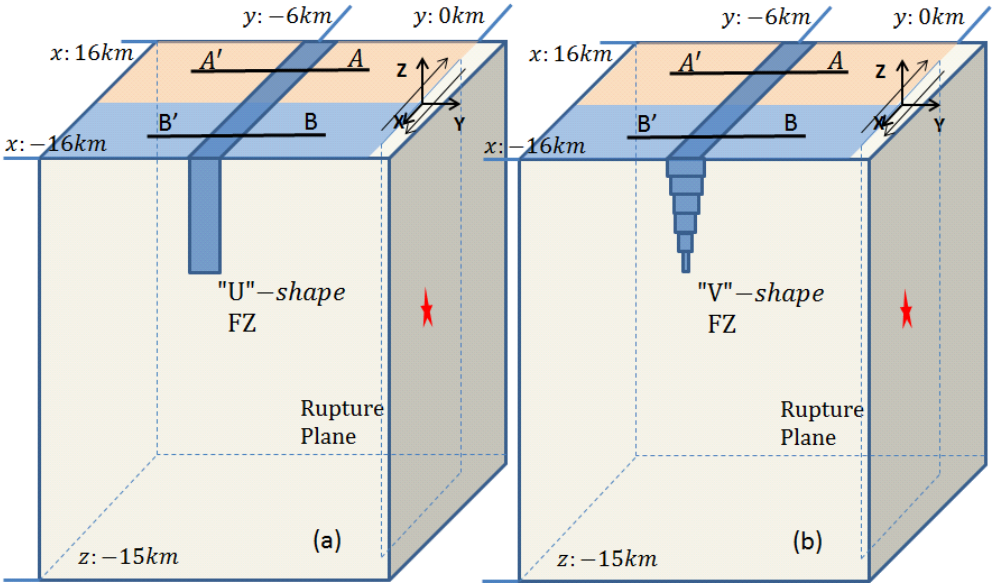

Figure 4. 1 The target model with (a) "U"-shape and (b) "V"-shape fault zone. The fault that ruptures in the model is 20 km long along strike and 15 km wide along dip. Rupture nucleates at the center of the fault plane, while the epicenter is the origin of the coordinate system. The center of compliant fault zone is 6 km away from the rupture fault. AA' and BB' are two profiles shown in Figure 4.2 and 4.3. As marked in the figure, AA' is in the compressive quadrant (orange color) where it experiences compressive change in the mean stress; while BB' is in the extensional quadrant (blue color) where it experiences extensional change in the mean stress. All the other parameters are the same in (a) and (b), except that the shape of the fault zone is gradually narrows from the free surface down to the bottom.

We conduct a series of experiments with "U"-shape fault zones of different widths and depths to explore the fault zone geometry effect on the displacement field (see Table 4.1 for fault zone geometry variation details). We also run simulations with "V"-shape (i.e., fault zone width decreases with depth) fault zones, to test the fault zone shape effect on the displacement field (Figure 4.1b and Table 4.1).

Table 4. 1 Compliant fault zone geometry and rigidity reduction property values tested in this study.

Fault zone shape	Geometry tests	
"U" shape fault zone	Depth (km)	2, 3, 6, 9, 12
	Width (km)	0.6, 1.2, 1.6 , 2.0, 2.4
	Seismic Wave velocity reduction	10%, 20%, 30%, 40%, 50%
"V" shape fault zone	6 km deep, width decreases with depth 40% seismic velocity reduction	

The material properties of the host rock are typical of crustal rocks, i.e., the P wave and S wave velocities are 6000 m/s and 3464 m/s, respectively, and density is 2670 kg/m3. Within the compliant fault zone, seismic velocities are reduced; while the density is the same as that of the host rocks (see Table 4.2 for material properties).

Table 4. 2 Material parameters

Material \ Parameters		Density (kg/m^3)	P-wave velocity (m/s)	S-wave Velocity (m/s)	tanϕ	C (MPa)
Elastic	Host rock	2670	6000	3464	0.75	1000
	Fault zone	2670	3600 (40% reduction)	2078 (40% reduction)	0.57	1000
Elastoplastic (Plastic)	Host rock	2670	6000	3464	0.75	10
	Fault zone	2670	3600 (40% reduction)	2078 (40% reduction)	0.57	1.5, 2.5, 3.5, 5

For each set of parameters, we simulate a pair of models, a target model and a reference model, to extract signals in the final displacement field that are associated with a pre-existing compliant fault zone. In the reference model of a given pair of models, the compliant fault zone is excluded, but otherwise the reference model is the same as the target model. By subtracting the displacement of the reference model from that of the target model, we obtain a residual displacement (e.g., Figure 4.2 and Figure 4.3), which characterizes the effect of the presence of the compliant fault zone on the displacement field.

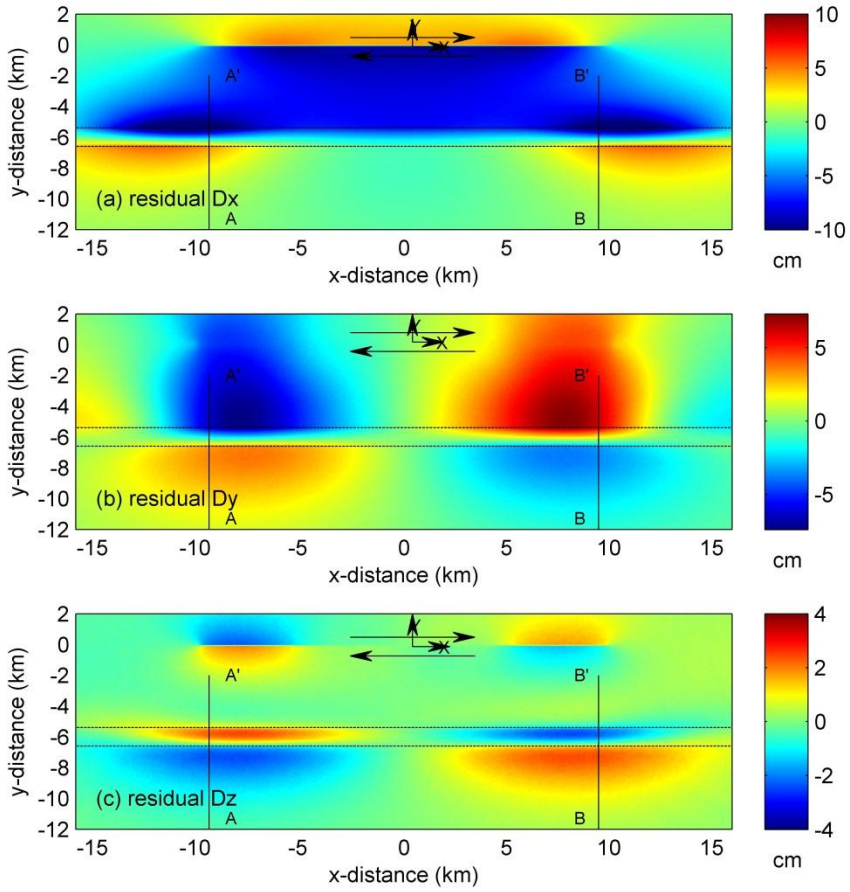

Figure 4. 2 Residual displacements (see text for definition) on the Earth's surface induced by an earthquake on a right-lateral strike-slip fault in a 3D elastic inhomogeneous media with a compliant fault zone. (a) fault-parallel (x) component Dx, (b) fault-normal (y) component Dy, (c) vertical (z) component Dz. Black arrows denote the right-lateral motion on the fault. Black dash lines delimit the fault zone. AA'(x= -9.5 km), BB'(x= 9.5 km) are the profiles shown in Figure 4.3. Fault zone is 3 km deep and 1.2 km wide in this model.

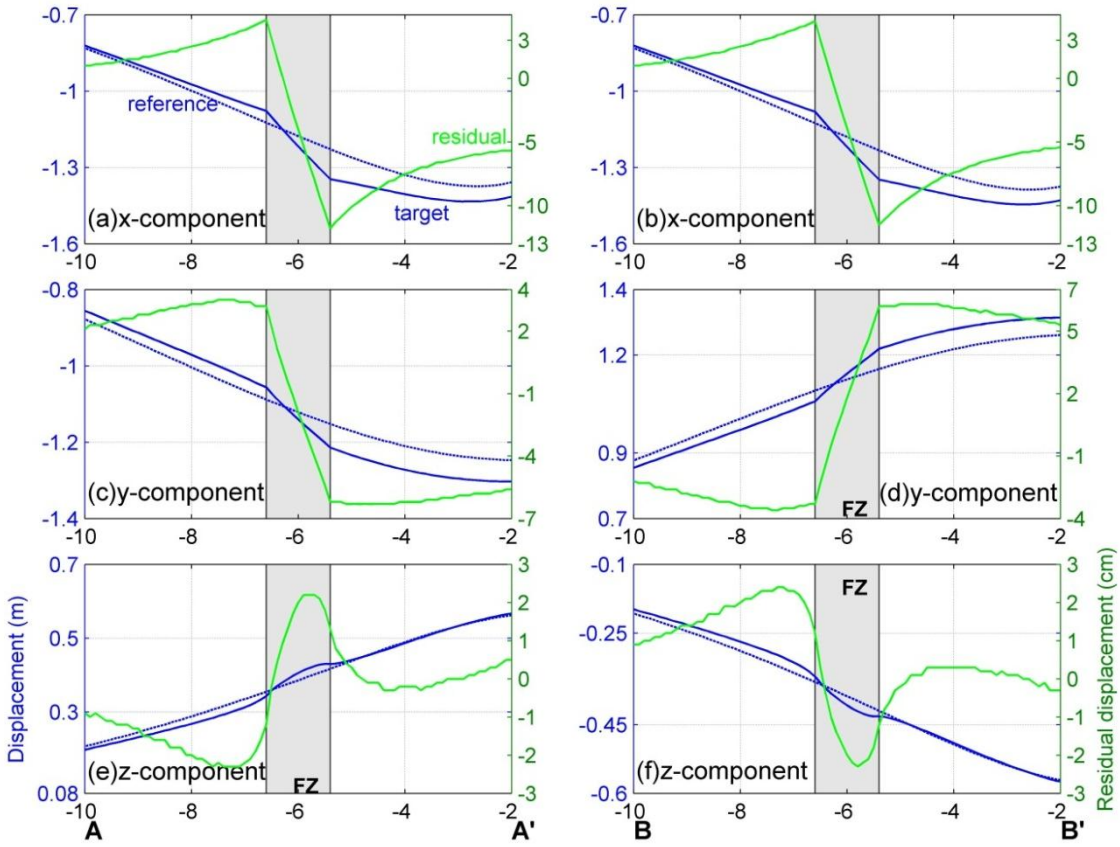

Figure 4. 3 Three displacement components along profiles AA' (a, c and e) and BB'(b, d and f) (see Figure 4.1 and Figure 4.2 for location). Residual displacement (green curve, in centimeter on the right axis) is calculated by subtracting static displacement (in meter on the left axis) of a reference model (dash blue) from that of the target model (solid blue). Shaded bands correspond to the width of fault zone (FZ). Fault zone is 3 km deep and 1.2 km wide in this model.

We use the Drucker-Prager yield criterion to characterize elastoplastic material behavior in the medium. This criterion [Drucker and Prager, 1952] requires that at a point in the medium, the stress condition satisfies:

$$\sqrt{0.5 s_{ij} s_{ij}} \leq -(\sigma_{kk}/3)\sin\varphi + c\cos\varphi \qquad (1)$$

Where s_{ij} is the deviatoric stress, σ_{kk} is the first invariant of the stress tensor, summation over repeated indices is assumed, c is cohesion and φ is the internal frictional angle. The left side of the equation is the square root of the second invariant of the deviatoric stress tensor, which is regarded as a measure of the shear stress in the 3D stress state. The right side of the equation is the yield stress. When the criterion is violated, stresses are adjusted to the yield level. The increments of plastic strain components at one time step $\delta\varepsilon_{ij}^{p}$ are calculated from the adjustment to the corresponding stress component and shear modulus [e.g., Duan and Day, 2008]. Following Ma [2008] and Ma and Andrews [2010], we use a scalar quantity η(t) to evaluate the accumulated inelastic strain due to yielding at time t with $\eta(0) = 0$ as follows:

$$\eta(t) = \eta(t - \Delta t) + \delta\eta\Delta t \ , \qquad \delta\eta = \sqrt{0.5(\delta\varepsilon_{ij}^{p} - \delta\varepsilon_{kk}^{p}/3)(\delta\varepsilon_{ij}^{p} - \delta\varepsilon_{kk}^{p}/3)} \ . \qquad (2)$$

We remark that this implementation of yielding criterion assumes no plastic volumetric deformation, which means $\delta\varepsilon_{kk}^{p} = 0$ in equation (2).

Elastoplastic calculations in the medium require the initial stress to be assigned to the entire model region. We set a depth-dependent pre-event stress field in this study. In our coordinate system, the x axis is parallel to the fault plane, the y axis is perpendicular to the fault plane (Figure 4.1), and the z axis is vertical. The vertical normal stress in the medium is set to be the lithostatic overburden minus the pore pressure, i.e., σ_{zz} = - (16.37 Mpa/Km) z, where z is the depth; while $\sigma_{xx}=1.25\sigma_{zz}$, $\sigma_{yy}=0.75\sigma_{zz}$ (stress is positive in tension). For shear stress, we assume $\sigma_{xy}= - 0.433\sigma_{zz}$, $\sigma_{xz}=\sigma_{yz}=0$.

We test the complete range of plastic parameters that allow plastic strain to occur. Details are discussed in Result section. We refer the models with plastic deformation as the plastic models; while we also use the same code to run the elastic models by setting a much higher value of cohesion (e.g., 10000 MPa) to avoid any plastic deformation from occurring. Elastic models are examined in this study primarily to serve for the following two purposes: 1, by comparing results from plastic models with those from elastic models, we enhance the illustration of the effects of inelastic response of compliant fault zone on the displacement field; 2, We explore the fault zone geometry, rigidity reduction effect on elastic inhomogeneous medium. All of the material parameters discussed above are summarized in Table 4.2.

In this study, we use a community verified finite element code EQdyna [e.g., Duan and Oglesby, 2006; Duan and Day, 2008; Harris et al., 2009, 2011; Duan, 2010a, 2010b; Duan et al., 2011] to perform numerical simulations of dynamic rupture on the fault and wave propagation in a 3D medium. A widely used slip weakening friction law [Ida., 1972; Andrews., 1976] is used to govern the rupture propagation on the fault. It assumes the frictional coefficient μ drops from static value μ_s to dynamic value μ_d linearly over the critical slip distance D_0, when shear stress on the fault reaches the yield stress. The fault edges (except at the free surface) are pinned by a high static frictional coefficient. To initiate the rupture, we prescribe a nucleation patch at the center of the fault plane, within which the rupture is forced to propagate at a fixed slow speed. Outside the nucleation patch, the rupture propagates spontaneously at faster speeds.

We run the dynamic simulations for 20 s, which is long enough for displacement field to reach the static value (Figure 4.4). The main part of the model is surrounded by a much larger buffer region. The buffer region is large enough to prevent reflections at artificial model boundaries from contaminating the simulation results. An elements size of 100 m in the main model region is used.

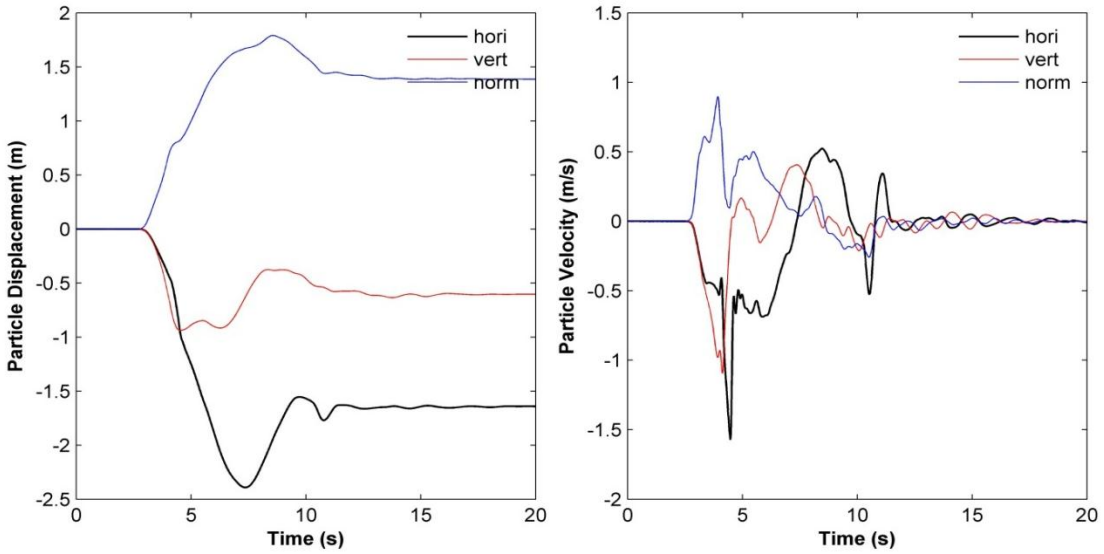

Figure 4. 4 Time history of particle displacement and particle velocity of one off-fault station with coordinates x = 10 km, y = - 6 km and z = 0 km from the target model. 20 second is long enough for the displacement field to reach the static solution.

4.3 Results

In this section, we primarily report results from two types of models. The first type of models is elastic models, where material responds to the dynamic rupture purely

elastically. In these models, we examine the effects on residual displacement field from fault zone geometry (i.e. width, depth and shape) and rigidity reduction property variations. In the second type, plastic strain is allowed to occur in the elastoplastic medium. Plastic parameters (internal friction tanφ and cohesion c) within fault zone material are set to be smaller than those from the host rocks in order to explore the effect from plastic strain on the residual displacement field. We test the complete range of plastic parameters that allow plastic strain to occur. In addition, we run models with fault zone geometry and shape variations in elastoplastic medium, to explore the combined effects from both the plastic strain and fault zone geometry and shape variations on residual displacement field.

4.3.1 Elastic models

In order to test the effect on residual displacement field from one specific parameter (i.e., fault zone depth, width, shape and rigidity reduction property), we design a serial of models, in each of that, only one of the above parameters is set to be different, otherwise is the same model as the others. For example, to test fault zone depth effect on the residual displacement field, we simulate the models with the same fault zone width, shape and rigidity reduction, but vary the fault zone depth extent. By displaying together the results from different models, we can observe the effect on the displacement field explicitly from the fault zone depth variation.

4.3.1.1 Fault zone depth and width effects on displacement field from elastic models

We focus on the set of models with "U"-shape fault zone, and seismic wave velocity for fault zone material has a 40% reduction compared with that of the intact rocks, to test the fault zone depth and width effects on the residual displacement field.

Figure 4.2 shows the residual displacement at the Earth's surface from a right-lateral strike slip fault system. It is calculated by subtracting the final displacement of the reference model from that of the target model (see Figure 4.3 for definition) in order to characterize the effect from the presence of a compliant fault zone on the displacement field. The fault-parallel component (Figure 4.2a) of residual displacement shows retro-grade motion (i.e., opposite to the long-term geologic slip) along the entire fault zone. The fault normal component (Figure 4.2b) exhibits compression over the fault zone in the compressive quadrant, and dilation in the extensional quadrant. The vertical component (Figure 4.2c) of residual displacement is enhanced by the presence of fault zone. In the compressive quadrant, the uplift is enhanced; while in the extensional quadrant, the subsidence is enhanced. A closer look of residual displacement in a profile view over AA' (in the compressive quadrant) and BB' (in the extensional quadrant) is displayed in Figure 4.3 (see Figure 4.1 and 4.2 for locations of AA' and BB'). Fault parallel residual displacement is symmetric in the compressive and extensional quadrants, while the fault normal and vertical residual displacements are anti-symmetric (i.e., opposite sense of motion, but same magnitude).

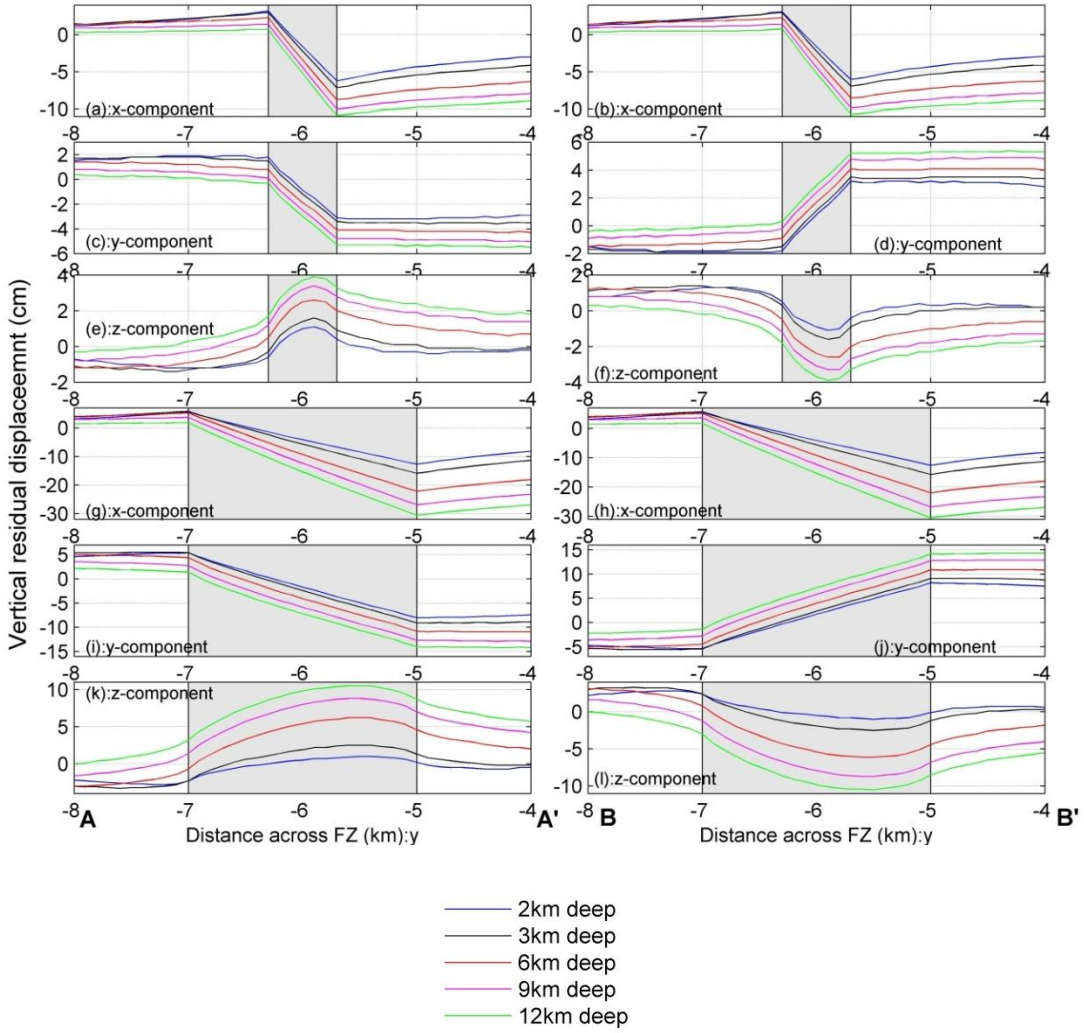

Figure 4. 5 Depth effect on surface residual displacement from elastic models. (a, c, e, g, i and k) residual displacements along profile AA' (see Figure 1 and 2 for location). (b, d, f, h, j and l) residual displacements along profile BB' (see Figure 1 and 2 for location). Shaded bands correspond to the width of the fault zone. Within each panel, 5 curves display the residual displacement profiles from 5 models with different depth extent. (a, b, c, d, e and f) are profiles from models with 0.6 km fixed width, while different depth extents. (g, h, i, j, k and l) are profiles from models with 2 km fixed width, while different depth extents.

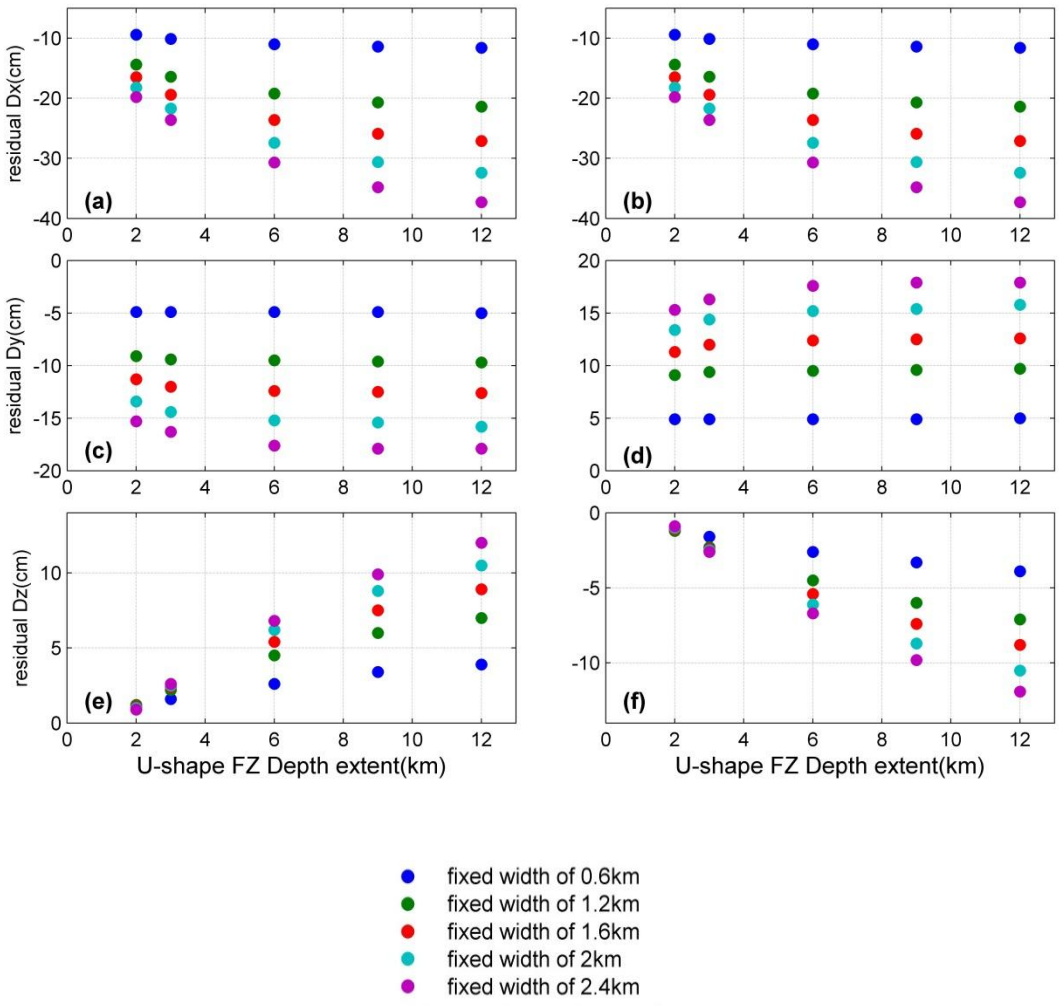

Figure 4. 6 Fault zone depth effects on the residual displacement field from elastic models. Relative horizontal residual displacement and peak values of vertical residual displacement across fault zone along profile AA'(a, c and e) and BB' (b, d and f) are displayed.

In this study, we tested 5 cases of fault zone depth extent, as of 2, 3, 6, 9, 12 km, respectively, and 5 cases of fault zone width, as of 0.6, 1.2, 1.6, 2 and 2.4 km, respectively (Table 4.1). Figure 4.5 shows fault zone depth effects on residual displacement in a profile view, with the two cases of 0.6 km and 2 km fixed fault zone

width, respectively. Relative horizontal residual displacement across fault zone and peak values of the vertical residual displacement along profile of AA’ and BB’ are collected and displayed in Figure 4.6. It is observed that the magnitude of fault-parallel and vertical residual displacements increase with fault zone depth, however, the results from wider fault zone are more responsive to the depth variation; while fault normal residual displacement tends to maintain the same value from the models with different fault zone depth extents.

Similarly, Figure 4.7 displays residual displacement from models with fixed fault zone depth and different widths in a profile view. Relative horizontal residual displacement and peak values of vertical residual displacement across fault zone along profile AA’ and BB’ are collected and showed in Figure 4.8. Residual displacement generally increases with fault zone width; however, for fault zones with shallow depth, vertical residual displacement tends to keep the same value, even decreases with fault zone width.

As the same set of data as showed in Figure 4.6 and Figure 4.8, but combined both the fault zone depth and width effects on residual displacement field, Figure 4.9 demonstrates combined effects of the fault zone width and depth on the residual displacement.

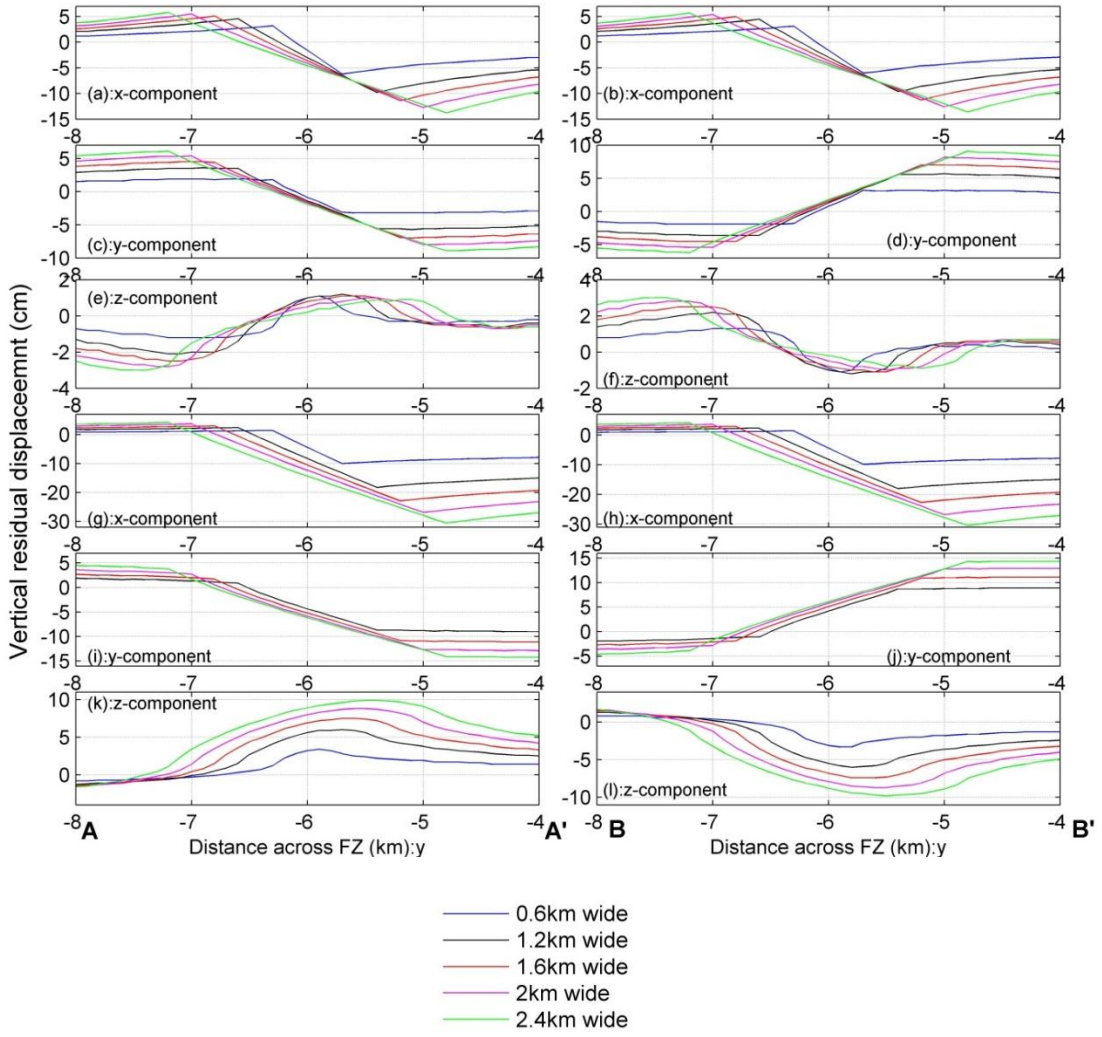

Figure 4. 7 Width effects on surface residual displacement from elastic models. (a, c, e, g, i and k) residual displacements along profile AA' (see Figure 4.1 and 4.2 for location). (b, d, f, h, j and l) residual displacements along profile BB' (see Figure 4.1 and 4.2 for location). Within each panel, 5 curves display the residual displacement profiles from 5 models with different widths. (a, b, c, d, e and f) are profiles from models with 2 km fixed depth extent, while different widths. (g, h, i, j, k and l) are profiles from models with 9 km fixed depth extent, while different widths.

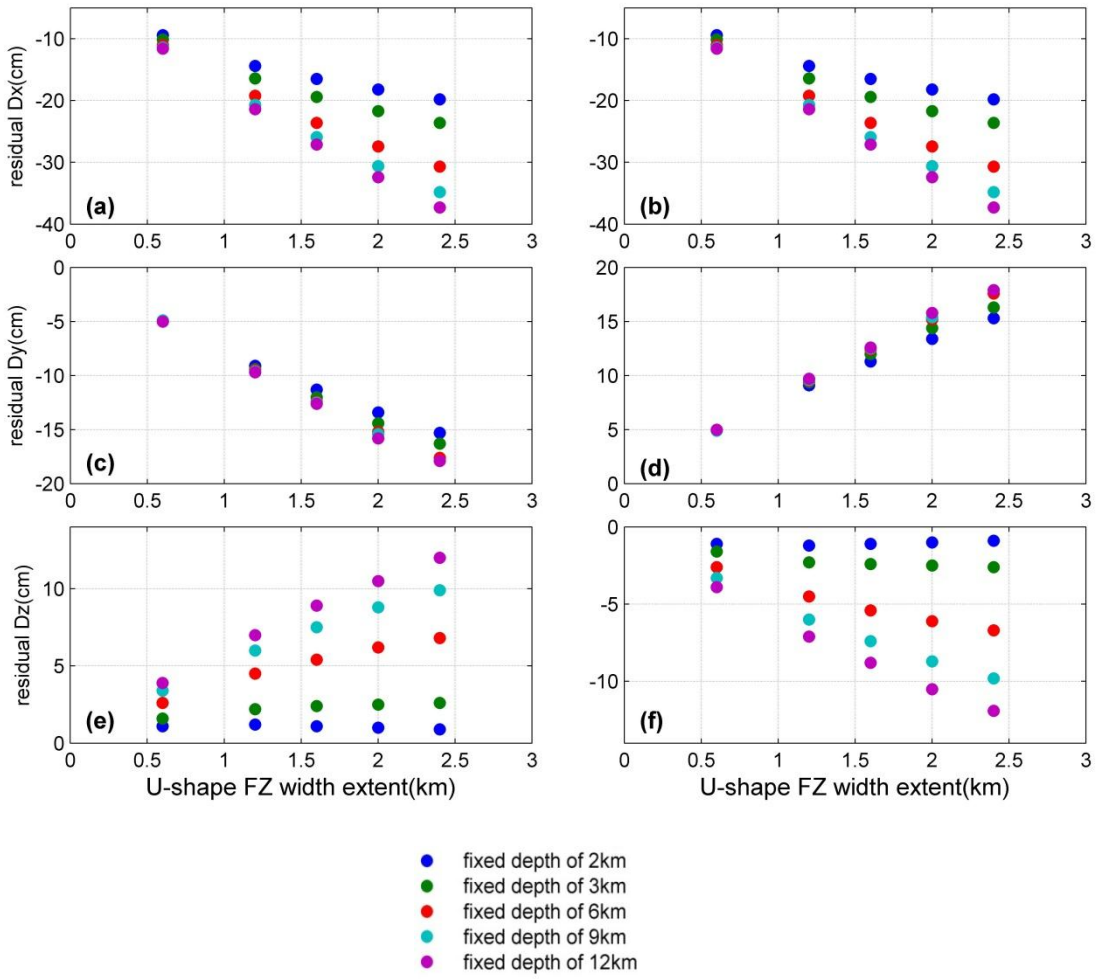

Figure 4. 8 Fault zone width effects on the residual displacement field from elastic models. Relative horizontal residual displacement and peak values of vertical residual displacement across fault zone along profile AA'(a, c and e) and BB' (b, d and f) are played.

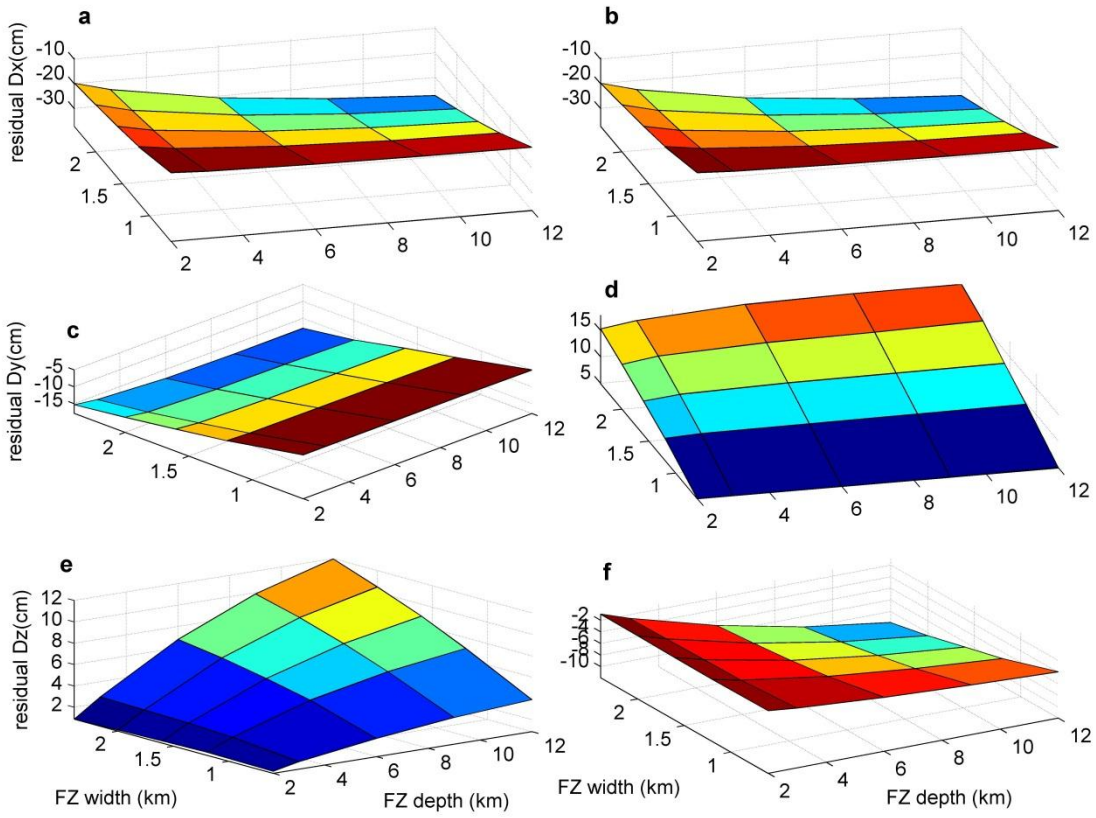

Figure 4. 9 Fault zone depth and width effects on residual displacement field from elastic models. Relative horizontal residual displacement and peak values of vertical residual displacement across fault zone along profile AA'(a, c and e) and BB' (b, d and f) are displayed.

4.3.1.2 Fault zone shape effect on displacement field from elastic model

Figure 4.1b shows the model with fault zone shape gradually narrows from the Earth's surface to the fault zone bottom, with 6 km depth extent, but 1.2, 1.0, 0.8, 0.6, 0.4, 0.2 km width at 0, 1, 2, 3, 4, 5, 6km depth extent, respectively. This gradually narrowing down "V"-shape of fault zone is reported to better fit the seismic observations [Ellsworth and Malin, 2006; Li et al, 2008; Cochran et al, 2009].

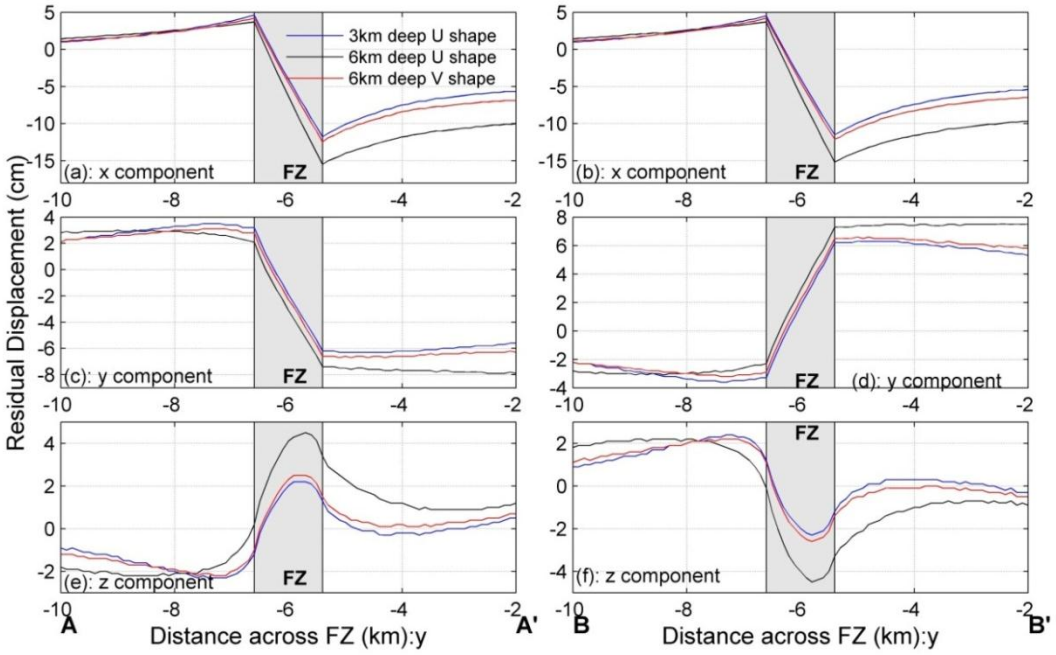

Figure 4. 10 Fault zone shape effect on surface residual displacement along profile AA'and BB' (see Figure 4.1b for location) from the elastic models. (a and b) Fault parallel component; (c and d) Fault normal component; (e and f) Vertical component. Shaded bands correspond to the near surface width of the fault zone.

Figure 4.10 display the residual displacement along profiles of AA' (a, c and e) and BB' (b, d and f) (see Figure 4.1b for location), respectively. Panels (a and b), (c and d), (e and f) show the fault-parallel, fault-normal and vertical residual displacements, respectively. In each panel, it displays three models with a fault zone width at the Earth's surface of 1.2 km, but different depth extents or fault zone shapes: 3km depth extent of "U"-shape fault zone (blue); 6km depth extent of "U"-shape fault zone (black); 6km depth extent of "V"-shape fault zone (red). By comparing the result from the "V"-shape fault zone with that from the "U"-shape fault zone model, we observe the following: 1)

the displacement anomaly across the fault zone only reflects the near surface fault zone width. The width of anomaly is clearly showed by the sharp change of the displacement curve across the fault zone, especially the horizontal residual displacement (Figure 4.10 a, b, c and d). Even though narrower widths are assigned at deeper depth with “V”-shape fault zone model, the width anomaly only reflects the near surface fault zone width, and does not give any information of width variation in depth. 2) The magnitude of residual displacement from “V”-shape fault zone model is closer to that of "U"-shape fault zone model with shallower depth (Figure 4.10 e and f). From an inversion perspective, it indicates that the “U”-shape fault zone and the “V”-shape fault zone may produce the similar magnitude of residual displacements that fit the observations. While the different choices of the fault zone model may lead to different understandings of the fault zone shape.

4.3.1.3 Fault zone rigidity reduction effect and the possible trade-off with fault zone width effect on residual displacement from elastic models

In this study, we explore several values of fault zone material rigidity reduction property (Table 4.1 and 4.2) to examine their effect on residual displacement field. Figure 4.11 (a, c and e) display the residual displacement from models with 3 km deep, 1.2 km wide “U”-shape fault zone, but with various seismic velocity reductions. The magnitude of residual displacement increases with the magnitude of seismic velocity reduction.

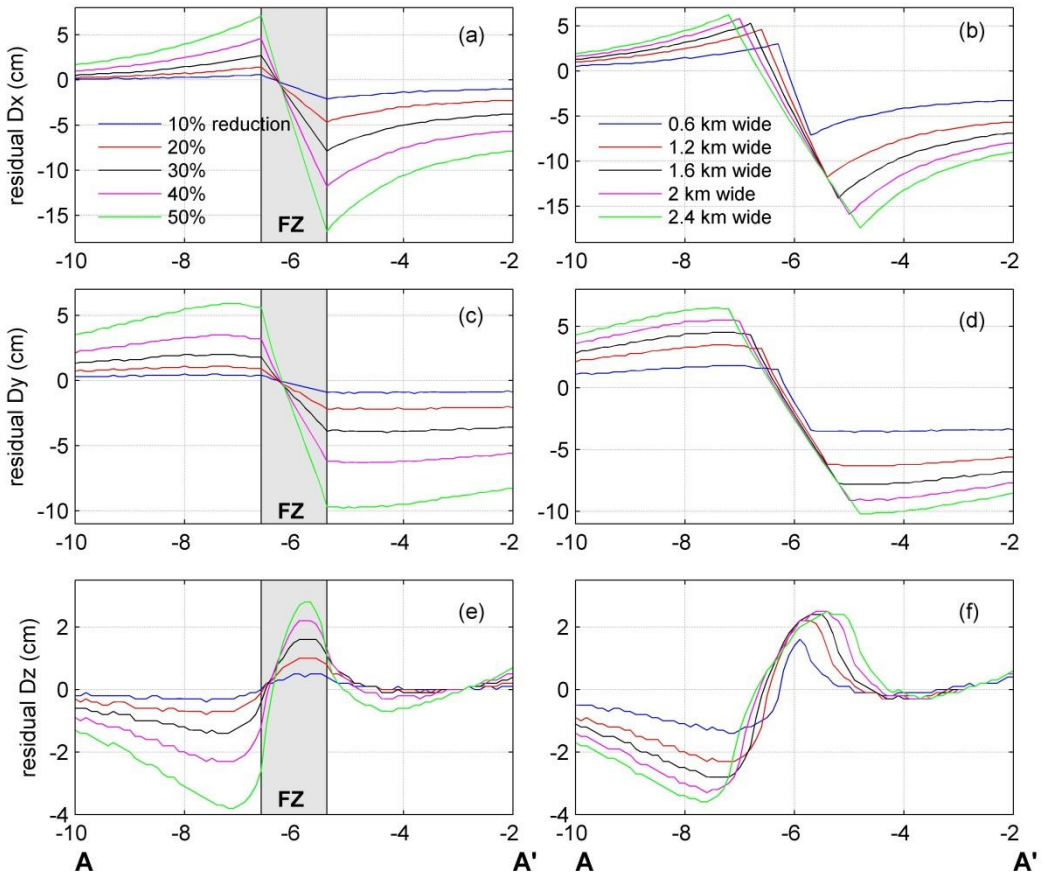

Figure 4. 11 Effect of fault zone seismic wave velocity reduction on the residual displacement (a, c and e) and the comparison with the effect of fault zone width on the residual displacement field (b, d and f). Models of "U"-shape fault zone of 3 km deep, 1.2 km wide, but various seismic wave velocity reductions are assumed in (a, c and d); While models of "U"-shape fault zone of 3 km fixed depth, 40% seismic velocity reduction, but various fault zone widths are assumed in (b, d and e).

We also provide the fault zone width effect on residual displacement in Figure 4.11 (b, d and f) from models with 3 km "U"-shape fault zone depth, 40% fault zone seismic velocity reduction, but various fault zone widths. There is a clear trade-off effect between the fault zone seismic velocity reduction property and the fault zone width on

residual displacement. For example, from an inversion perspective, to fit some observation of relatively large residual displacement (e.g., the green curves in Figure 4.11), one can either using a fault zone model with 50% seismic velocity reduction property, but 1.2 km, relatively narrower fault zone width, or one can choosing fault zone models of relatively smaller (i.e., 40% seismic velocity reduction), but wider fault zone (i.e., 2.4 km wide). Both the above mentioned models have the same fault zone shape and depth of 3 km, but with different choices of controlling parameter (i.e., rigidity reduction vs. fault zone width) in the models, it may result in different understanding of the fault zone width and rigidity reduction property.

4.3.2 Plastic models

4.3.2.1 Plastic parameter choices

In this study, experiments are conducted to explore in details the range of plastic parameter (i.e., internal friction coefficient tanφ and cohesion c) choices which allow plastic yielding to occur. As discussed in the previous 2D and 3D studies [Duan, 2010a; Duan et al, 2011; Kang and Duan, 2013], the plastic strain only occurs when the initial prestress value is close to yielding. Thus, the plastic parameters are chosen to make the yielding strength close to, and a little larger than the shear stress.

As stated in the 4.2 Methods and Models section, we use slip weakening law to control the rupture propagation, and the depth dependent initial stress in the model. The initial stress state is assumed uniform in the entire working region, the maximum principle stress is optimal (i.e., 30° to fault plane). Once the initial stress is set, the square root of second invariant of deviatoric stress, which is a measure of the shear

stress state, will follow the blue line as in Figure 4.12. Drucker-Prager criterion is used in this study to capture the material plastic yielding behavior. As listed as right hand side of equation (1) in 4.2 Method and Model section, the mean stress condition (fixed once the initial stress values assigned) and the values of internal friction coefficient tanφ and cohesion c determine the yielding strength with the given initial stress state. Thus, one can explore the choices of plastic parameters (i.e., internal friction coefficient tanφ and cohesion c) to make yielding strength line close to the shear stress line.

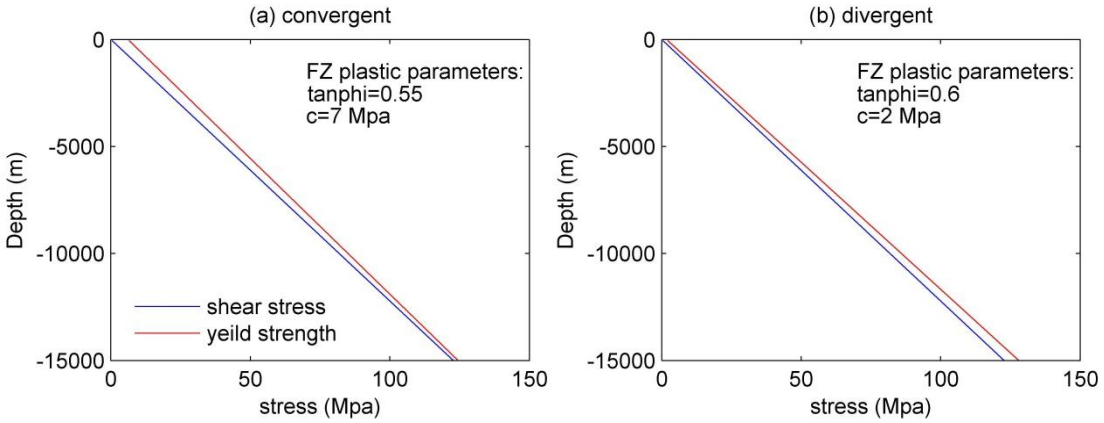

Figure 4. 12 Different choices of internal frictional angle have different impact on the yielding strength. (a) Yielding strength is convergent to the shear stress line; (b) yielding strength is divergent to the shear stress line.

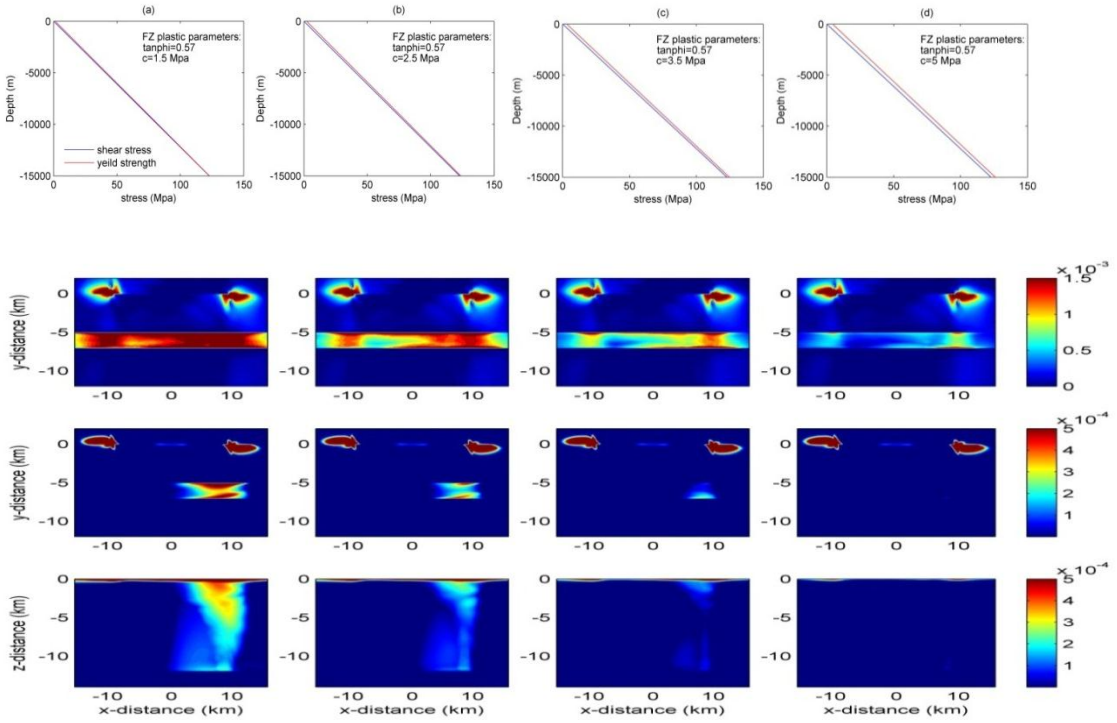

Figure 4. 13 Fault zone plastic parameters effect on plastic strain distribution. All the four cases have the same tanφ as 0.57, while with different cohesion values of: (a) 1.5 MPa; (b) 2.5 MPa; (c) 3.5 MPa; (d) 5 MPa, respectively. The subpanels from top to bottom are: initial shear stress and fault zone yielding strength along with depth; plastic strain distribution on the Earth's surface; plastic strain distribution on a horizontal plane at depth of z = - 2 km; plastic strain distribution on a vertical plane along the center of the fault zone (y = - 6 km).

In the initial stress field discussed above, it is observed that the choice of tanφ = 0.577 (not shown), makes the yielding strength parallel to the shear stress line; the choice of tanφ <0.577 leaves yielding strength line convergent (closer) to the shear stress line with increase of depth (Figure 4.12 a); While the choice of tanφ>0.577 gives rise of yielding strength line divergent (further away) to the shear stress line with depth (Figure 4.12 b). It suggests that if tanφ values are bigger than 0.577 for the fault zone material,

there will not be any pre-event yielding (i.e., yielding in the initial stress field before dynamic rupture propagates) even with material cohesion is set as low as 0 MPa for the fault zone material. However, with tanφ value of 0.577 or less for fault zone material, it requires adjustments of the fault zone cohesion value accordingly in order to avoid the pre-event yielding within the fault zone. The divergent and convergent trends do not have a direct physical meaning, but the rule of thumb is that the closer the shear stress to the yielding strength, the larger the plastic strain may occur.

Figure 4.13 (a-d) show four cases of plastic parameter choices and the final plastic strain distribution on different planes. In all four cases, initial stress condition is the same, fault zone tanφ is set to be 0.57, but the cohesion value equals to 1.5, 2.5, 3.5 and 5 MPa, respectively. The plastic strain distribution follow the same pattern that it occurs along the entire fault zone near the Earth's surface, and only at the extensional quadrant at depth. However, the magnitude of the plastic strain is smaller when fault zone material is stronger with larger cohesion. When cohesion value equals to 5 MPa, with tanφ as 0.57, there is little plastic strain at depth; while still certain amount of plastic strain occurring near the Earth's surface. However, the magnitude of that plastic strain is small, which only causes difference in the vertical residual displacement at the millimeter scale, compared with purely elastic model, which hardly makes any first order effect on the surface residual displacement result. In general, smaller values of both tanφ and c can give a weaker material that will be more susceptible to inelastic deformation.

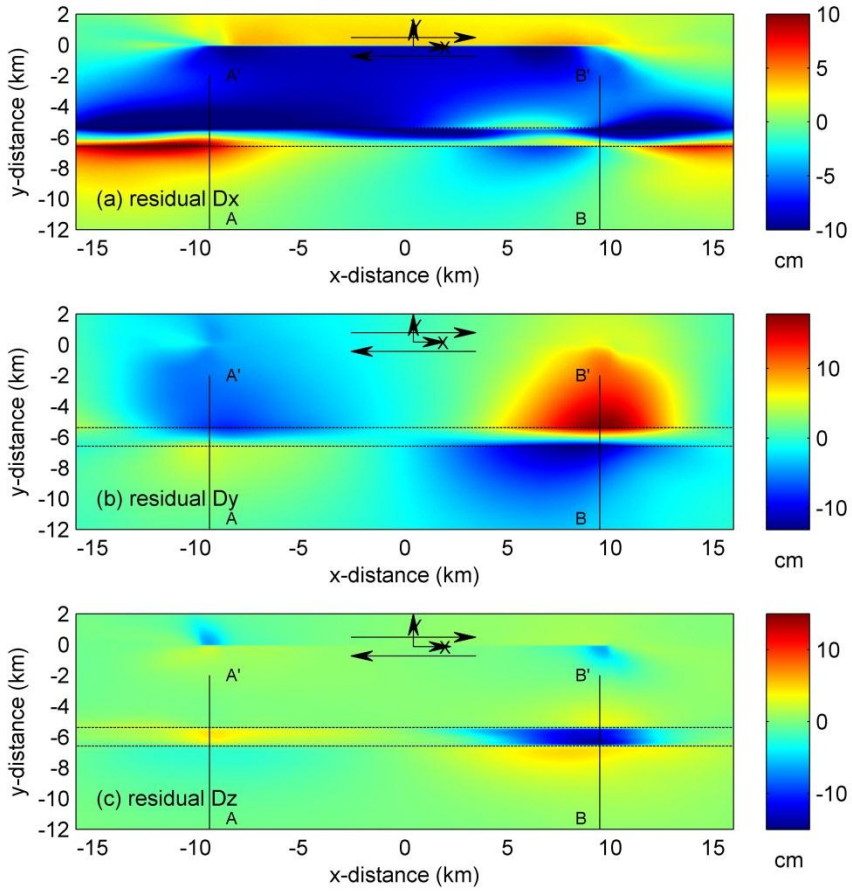

Figure 4. 14 Residual displacements (see text for definition) on the Earth's surface induced by an earthquake on a right-lateral strike-slip fault in a 3D elastoplastic inhomogeneous media with a compliant fault zone. (a) fault-parallel (x) component Dx, (b) fault-normal (y) component Dy, (c) vertical (z) component Dz. Black arrows denote the right-lateral motion on the fault. Black dash lines delimit the fault zone. AA'(x=-9.5 km) and BB' (x=9.5 km) are two profiles shown in Figure 4.15 and Figure 4.17.

Residual displacement on the Earth's surface is displayed in Figure 4.14 of fault-parallel (a), fault normal (b) and vertical (c) component, respectively. The fault zone model used to produce the residual displacement in Figure 4.14 has the plastic

parameters of tanφ = 0.57 and c = 2.5 MPa from 3 km deep, 1.2 km wide "U"-shape fault zone. This set of plastic parameters gives moderate magnitude of plastic strain in the modeling results, avoiding the end member scenarios. Thus this set of plastic parameter will be used in the following plastic models as a representative case to explore other features introduced by inelastic deformation.

4.3.2.2 Fault zone depth and width effects on displacement field from plastic models

Same as in the elastic models, we focus on the set of models with "U"-shape fault zones, and seismic wave velocity for fault zone material has a 40% reduction compared with that of the intact rocks, to test the fault zone depth and width effect on residual displacement field in plastic models. Plastic parameters of tanφ = 0.57 and c = 2.5 MPa are used in all the following plastic models.

Figure 4.14 shows an example of the residual displacement at the Earth's surface from plastic models with 3 km deep, 1.2 km wide "U"-shape fault zone. Compared with residual displacement from the elastic models with the same fault zone geometry in Figure 4.2, the magnitude of residual displacement in Figure 4.14 increases slightly in the compressive quadrant, due to the plastic strain occurs near the Earth's surface because of the low confining stress at shallow depth; while for the residual displacement in the extensional quadrant, the magnitude of fault-normal and vertical residual component increases dramatically compared with the elastic model. For fault-parallel component, some portion of fault zone exhibits sympathetic motion (i.e., consistent to the long-term geologic slip), while the remaining portion still shows retro-grade motion (i.e., opposite to the long-term geologic slip) across the fault zone. The dramatic changes

in the extensional quadrant are due to the extensive plastic strain occurs both near the Earth's surface and at deeper depth within fault zone.

We explore the same depth and width variations in plastic models as in the elastic models (Table 4.1). Figure 4.15 shows fault zone depth effect on residual displacement in a profile view, with the two representative cases of 0.6 km and 2 km fixed fault zone width, respectively. Relative horizontal residual displacement across fault zone and peak values of vertical residual displacement along profile of AA' and BB' (see Figure 4.1 and 4.14 for locations) are collected and displayed in Figure 4.16. In the compressive quadrant (Figure 4.16 a, c and e), the trend of fault zone width effect on the residual displacement is similar to that in the elastic model: the magnitude of fault-parallel and vertical residual displacement increases with fault zone depth, however, the results from wider fault zone are more responsive to the depth variation; while fault normal residual displacement tends to maintain the same value from the models with different fault zone depth extents. While in extensional quadrant (Figure 4.16 b, d and f), the magnitude of residual displacement generally increases with fault zone depth, however the trend is no longer fitted by a linear relationship. Notice that the relatively narrower fault zones are more likely to have sympathetic motion in fault parallel residual displacement.

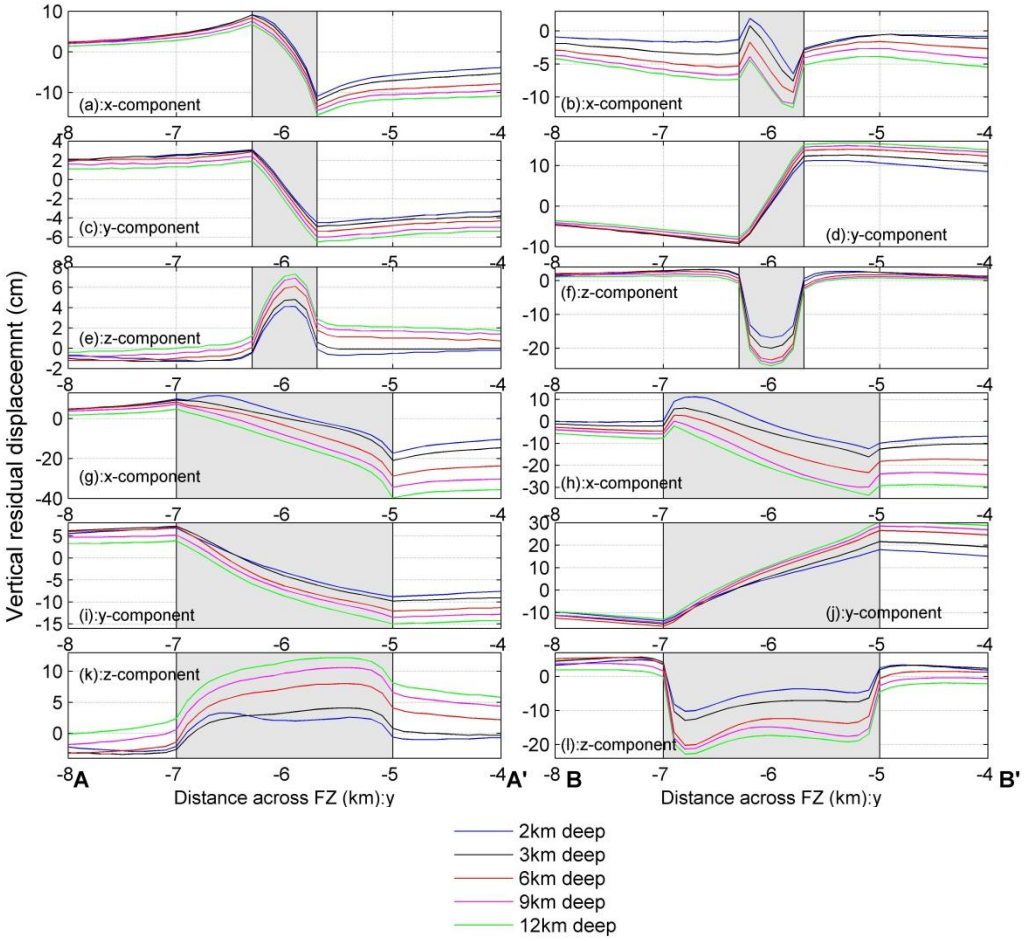

Figure 4. 15 Depth effects on the surface residual displacement from plastic models. (a, c, e, g, i and k) residual displacements along profile AA' (see Figure 1 and 2 for location). (b, d, f, h, j and l) residual displacements along profile BB' (see Figure 1 and 2 for location). Shaded bands correspond to the width of the fault zone. Within each panel, 5 curves display the residual displacement profiles from 5 models with different depth extent, otherwise is the same as each other. (a, b, c, d, e and f) are profiles from models with 0.6 km fixed width, while different depth extents. (g, h, i, j, k and l) are profiles from models with 2 km fixed width, while different depth extents.

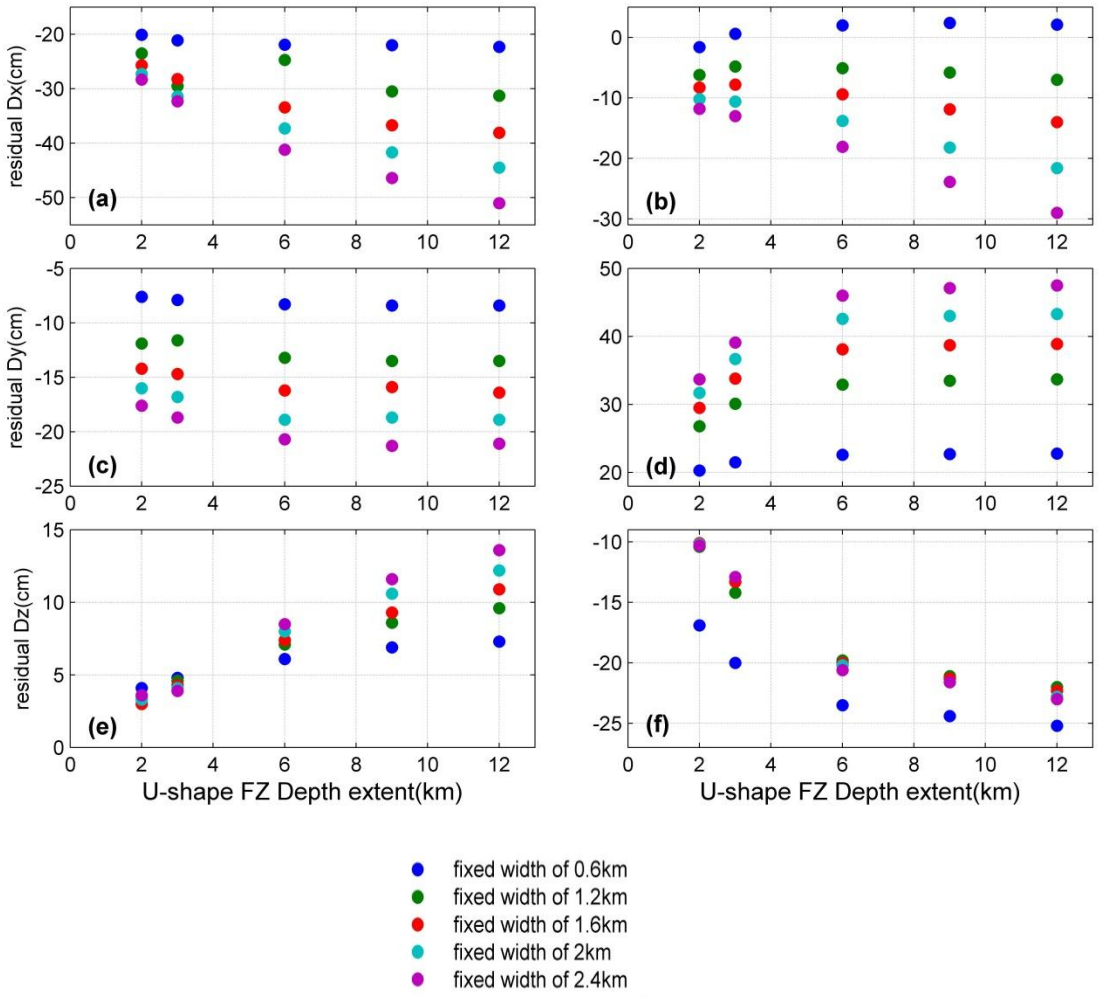

Figure 4. 16 Fault zone depth effects on the residual displacement field from plastic models. Relative horizontal residual displacement and peak values of vertical residual displacement across fault zone along profile AA'(a, c and e) and BB' (b, d and f).

Similarly, Figure 4.17 displays residual displacement from models with different fault zone widths in a profile view. Relative horizontal residual displacement and peak values of vertical residual displacement across fault zone along profile AA' and BB' (see Figure 4.1 and 4.14 for locations) are collected and showed in Figure 4.18. Horizontal

residual displacement generally increases with fault zone width; while the fault zone width effect on vertical residual displacement shows some complexities: in the compressive quadrant, vertical residual displacement from relatively shallower fault zones tends to keep the same value, even decreases with fault zone width. The vertical residual displacement from relatively deeper fault zones increases with fault zone width. In the extensional quadrant, the largest magnitude of vertical residual displacement always occurs in the fault zone with the narrowest width, regardless of the fault zone depth extent.

As the same set of data as showed in Figure 4.16 and Figure 4.18, but combined both the fault zone depth and width effects on residual displacement field, Figure 4.19 demonstrates combined effects of the fault zone width and depth on the residual displacement.

All the changes of residual displacement in plastic models are due to the plastic strain occurred near the Earth's surface along the entire fault zone and at deeper depth in the extensional quadrant within fault zone. Figure 4.20 compares the plastic strain distribution on (a and b) the Earth's surface, (c and d) a horizontal plane at 2km depth (z=-2km), (e and f) a vertical plane at the middle of the fault zone (y=-6km), from the plastic models with 12 km deep, but 1.2 and 2 km wide fault zone, respectively. It suggests that from the same rupture source, it will result in larger plastic strain within narrower fault zone than within the wider fault zone. That explains why we observe larger magnitude of vertical residual displacement and sympathetic motion in fault

parallel residual displacement in the extensional quadrant within relatively narrower fault zones.

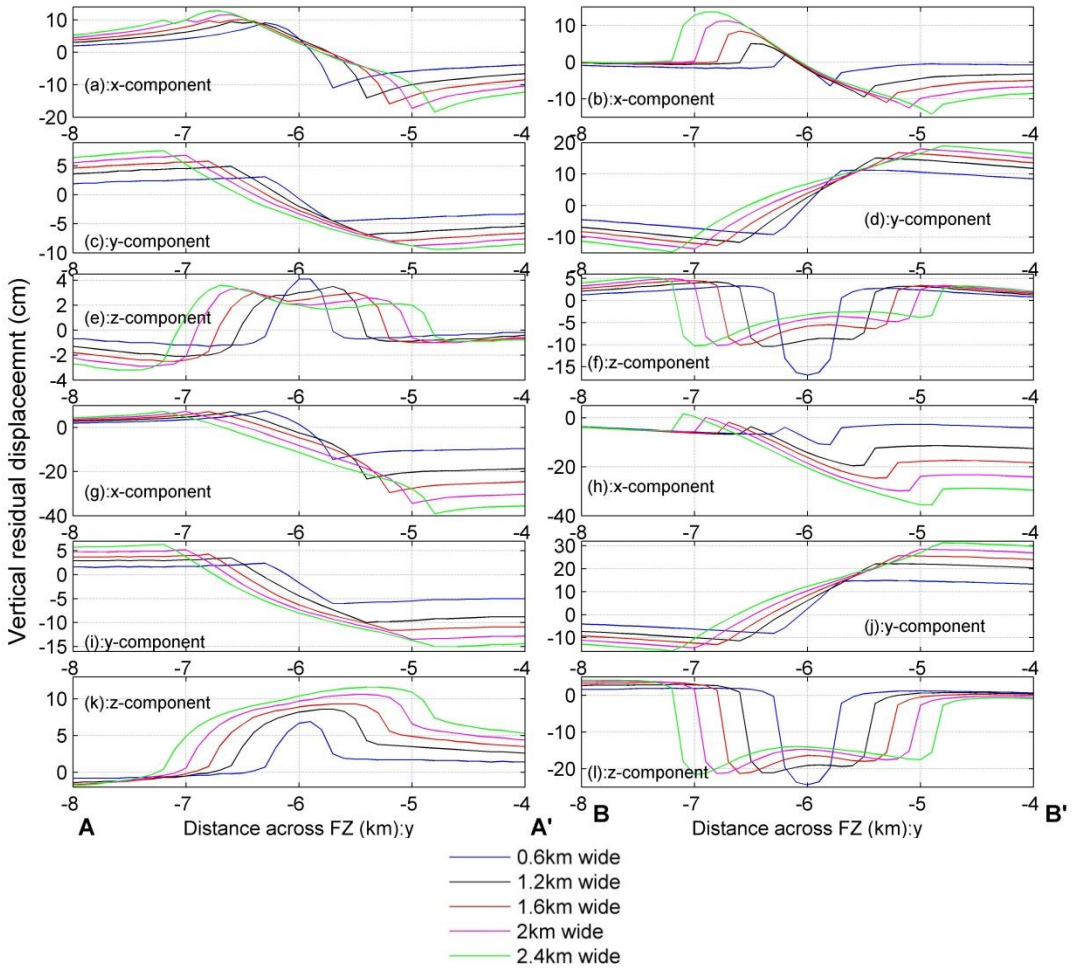

Figure 4. 17 Width effects on the surface displacement from plastic models. (a, c, e, g, i and k) residual displacements along profile AA' (see Figure 1and 2 for location). (b, d, f, h, j and l) residual displacements along profile BB' (see Figure 1 and 2 for location). Within each panel, 5 curves display the residual displacement profiles from 5 models with different depth extent, otherwise is the same as each other. (a, b, c, d, e and f) are profiles from models with 2 km fixed depth extent, while different widths. (g, h, i, j, k and l) are profiles from models with 9 km fixed depth extent, while different widths.

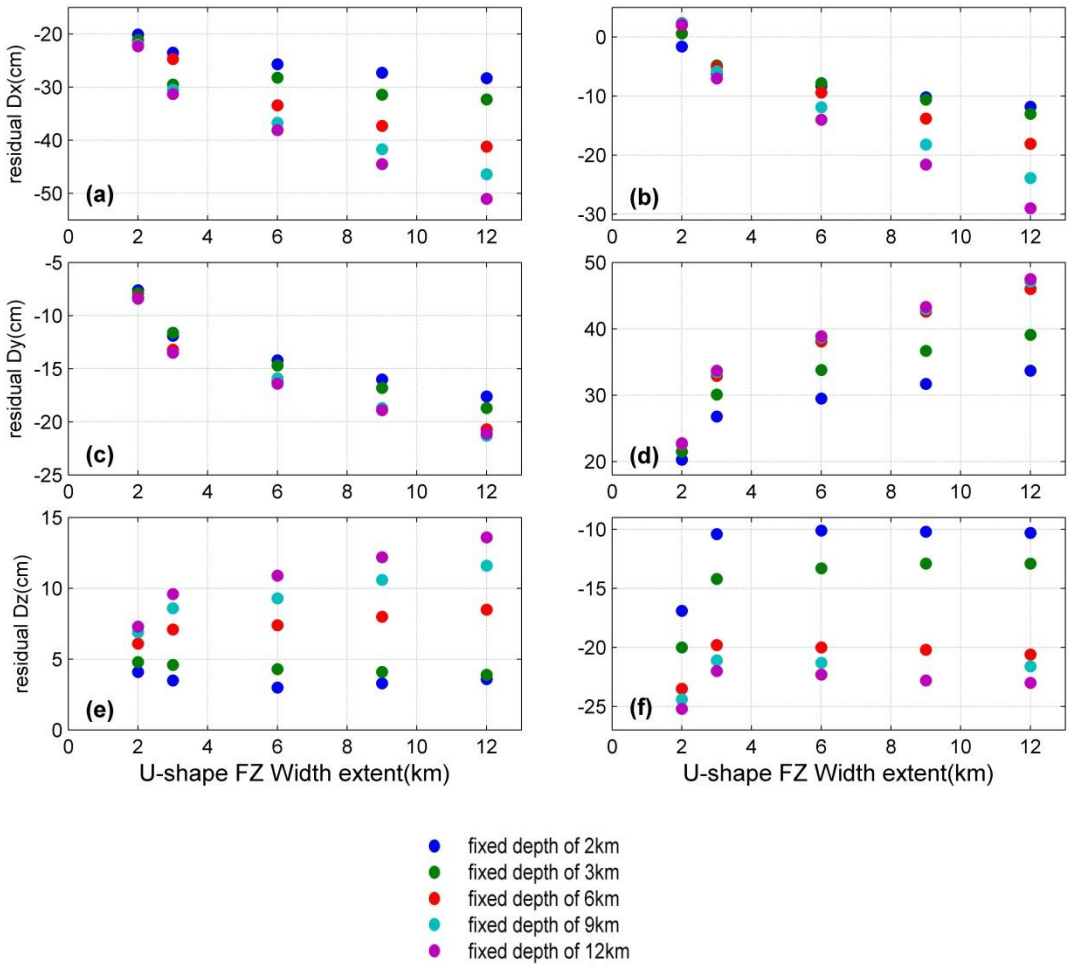

Figure 4. 18 Fault zone width effects on the residual displacement field from plastic models. Relative horizontal residual displacement and peak values of vertical residual displacement across fault zone along profile AA'(a, c and e) and BB' (b, d and f).

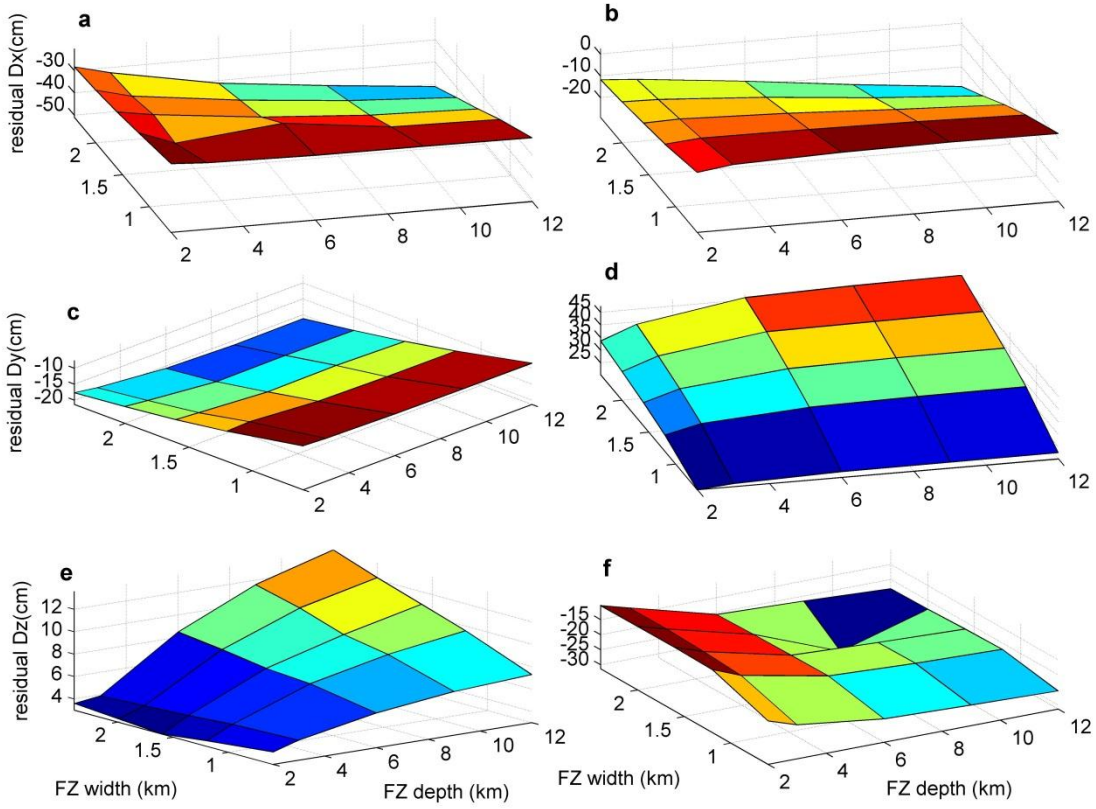

Figure 4. 19 Fault zone depth and width effects on residual displacement field from plastic models. Relative horizontal residual displacement and peak values of vertical residual displacement across fault zone along profile AA' (a, c and e) and BB' (b, d and f).

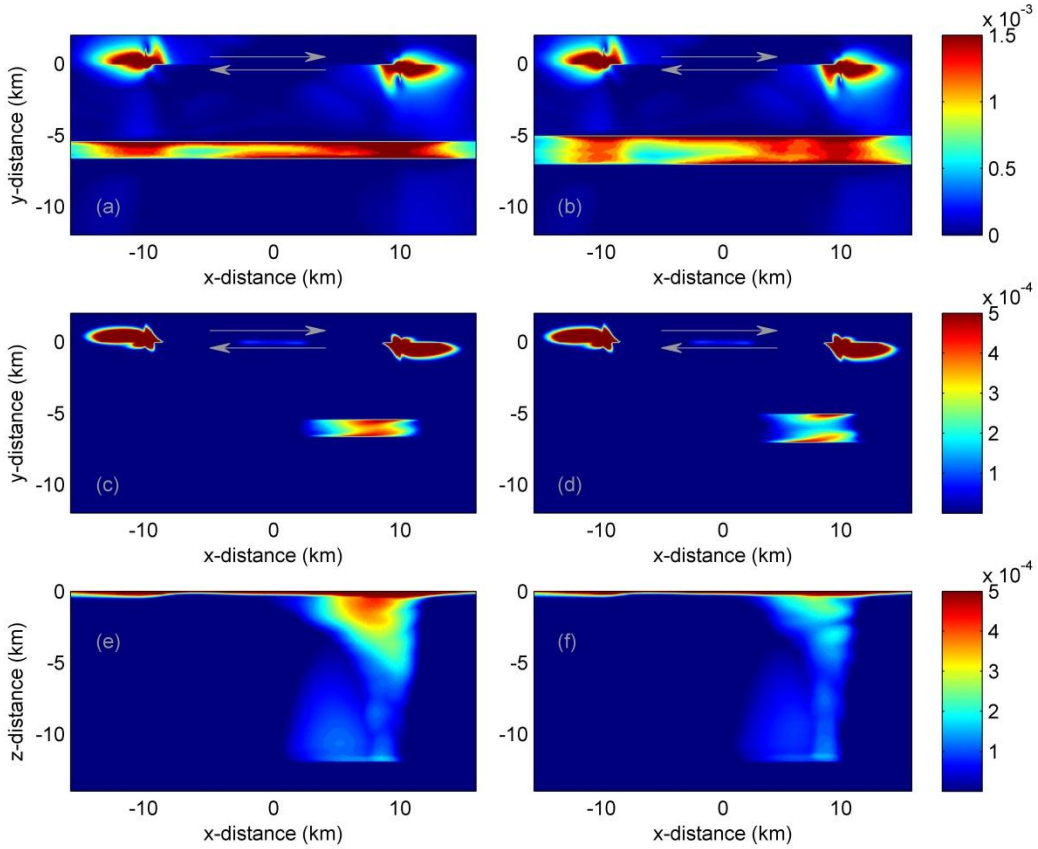

Figure 4. 20 Plastic distribution on (a and b) the Earth's surface, (c and d) a horizontal plane at 2km depth (z=-2km), (e and f) a vertical plane at the middle of the fault zone (y=-6km), from the plastic model with 12 km deep, but 1.2 and 2 km wide fault zone, respectively.

4.4 Discussion

Although it has long been recognized that material can behave inelastically in response to earthquake shaking [e.g., Kramer, 1996; Vidale and Li, 2003], the importance of plastic deformation to dynamic rupture simulation has also been explored by seismologists in the past decade [e.g., Andrews, 2005; Duan, 2008a; Duan and Day, 2008; Ma, 2008; Ma and Andrews, 2010], geodetic studies [e.g., Fialko et al, 2002;

Fialko, 2004; Barbot et al, 2009] still consider fault zones respond elastically to nearby large earthquakes, partly because it is hard to directly distinguish inelastic response from elastic one from the observed data.

Duan and co-workers have studied the inelastic response of compliant fault zones to nearby earthquakes and its effects on the displacement field in strike-slip faulting models in both 2D and 3D [Duan, 2010a; Duan et al, 2011; Kang and Duan, 2014]. They report the main features of three dimensional plastic strain distribution and its effect on the displacement field. Their results from previous 2D and3D plastic models suggest that inelastic response of a compliant fault zone with a certain level of plastic deformation can result in sympathetic motion across a strike-slip fault zone exhibited in the fault-parallel horizontal displacement, while elastic response results in retrograde motion [e.g., Fialko et al., 2002]. This contrast can be directly used to distinguish the two types of response.

However, as discussed earlier, magnitude of plastic strain is determined by plastic parameters of internal friction tanφ and cohesion c, as showed in equation (1) in 4.2 Methods and Models section. If fault zone rocks have a relatively large tanφ and/or a large cohesion, the magnitude of plastic strain can be small, thus the sympathetic motion may be not obvious or even disappear. Instead, one may observe reduced retro-grade motion in fault parallel residual displacement. At the same time, the reduced retro-grade motion can be also from a narrower, shallower fault zone segment or from a fault zone segment with smaller rigidity reduction property in an elastic inhomogeneous model. However, we can still distinguish inelastic response from elastic response by examining

the fault-parallel horizontal displacement in the conjunction with the vertical displacement: compared with purely elastic response, weak inelastic response causes reduced retrograde fault-parallel motion while enhanced vertical motion.

For example, Figure 4.21 shows the surface residual displacement from the 3km deep, 1.2 km wide, "U"-shape fault zone model, with the plastic parameter within fault zone of $\tan\varphi=0.57$, cohesion=3.5 MPa. Other parameters are the same as the model in Figure 4.14. Figure 4.22 and Figure 4.23 show 8 profiles (see Figure 4.21 for locations) of fault-parallel and vertical residual displacements, respectively. Especially, area where profiles of EE', FF' and GG' go through, it exhibits the reduced retro-grades motion in the fault-parallel horizontal residual displacement; while it shows the enhanced subsidence compared with that from the purely elastic model. In other words, if plastic strain does occur, with the conjunction of the above two residual displacement components (i.e., fault-parallel horizontal component and vertical component), one may distinguish the two types of response solely from the residual displacement field without knowledge of material properties. It may further provide constrains to the absolute stress level within the fault zone, since plastic yielding only occurs when material is already close to failure before the earthquake.

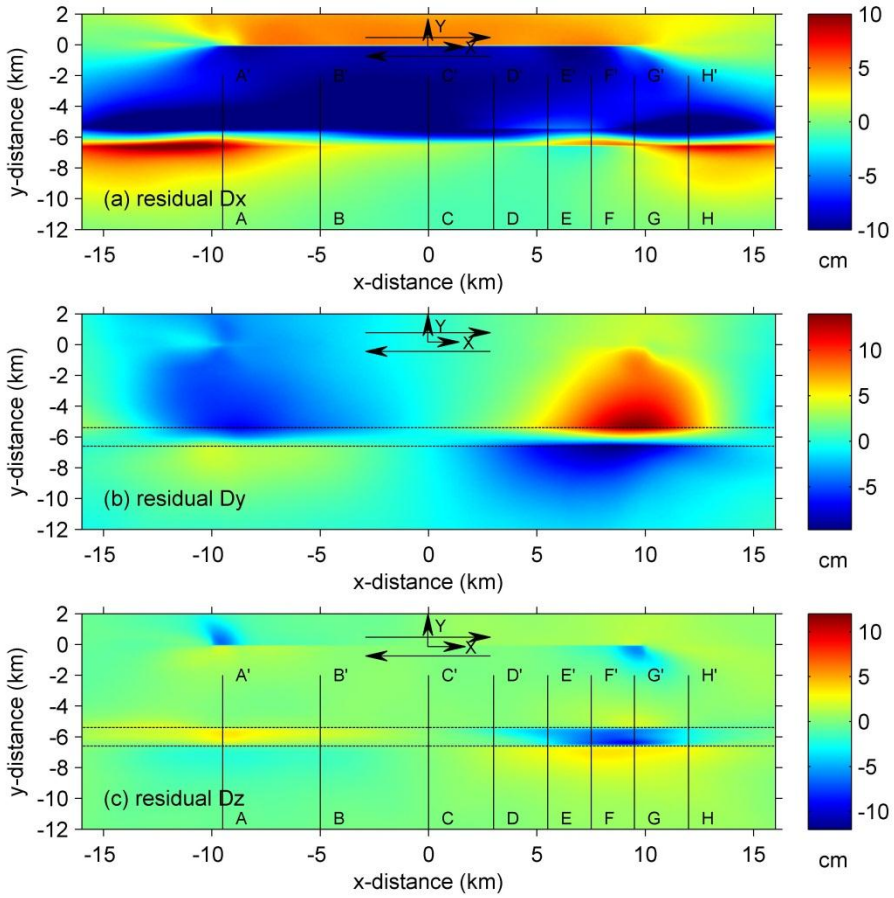

Figure 4. 21 Residual displacements on the Earth's surface induced by an earthquake on a right-lateral strike-slip fault in a 3D elastoplastic inhomogeneous media with a compliant fault zone (plastic parameter: tanφ = 0.57 and c = 3.5 MPa). (a) fault-parallel (x) component Dx, (b) fault-normal (y) component Dy, (c) vertical (z) component Dz. Black arrows denote the right-lateral motion on the fault. Black dash lines delimit the fault zone. AA'(x= -9.5 km), BB' (x= -5 km) , CC' (x= 0 km) , DD' (x= 3 km) , EE' (x= 5.5 km) , FF' (x= 7.5 km) , GG' (x= 9.5 km) and HH' (x= 12 km) are the profiles shown in Figure 4. 22 and Figure 4.23.

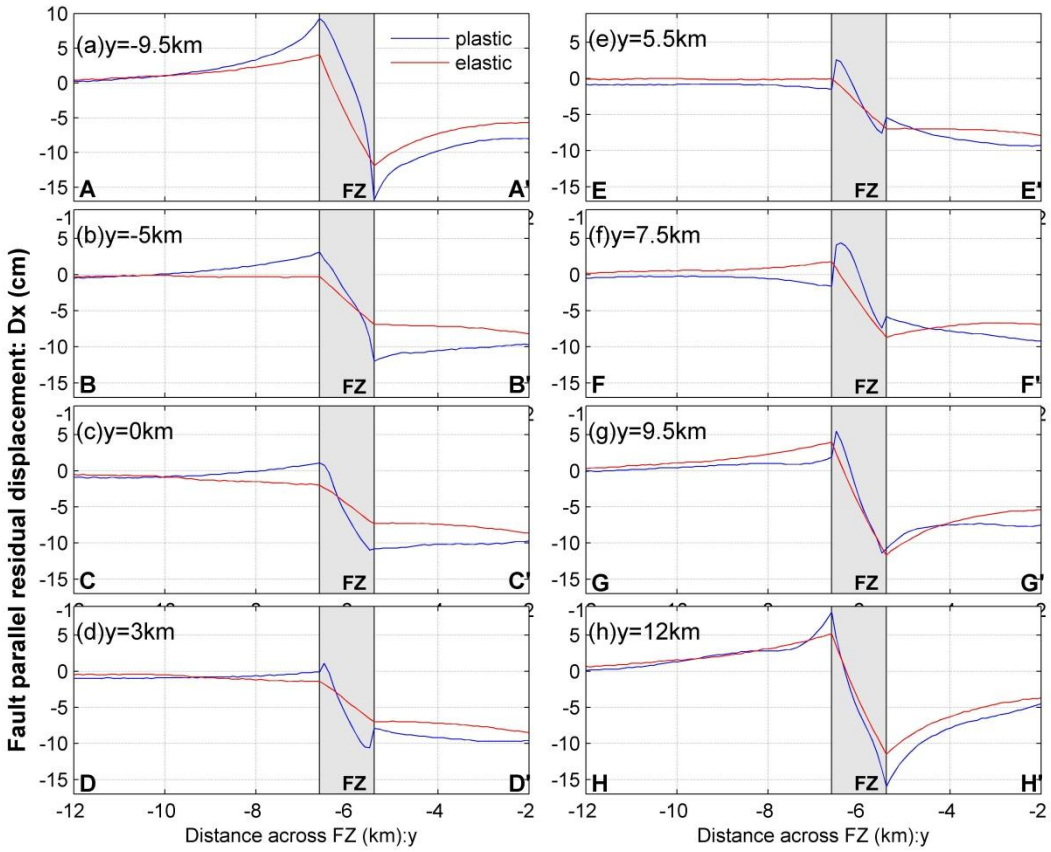

Figure 4. 22 Fault-parallel horizontal residual displacements along 8 profiles (locations in Figure 4.21). The blue curves are profiles from the plastic model in Figure 4.21. The red curves are profiles from the elastic model for comparison. Shaded bands correspond to the width of the fault zone.

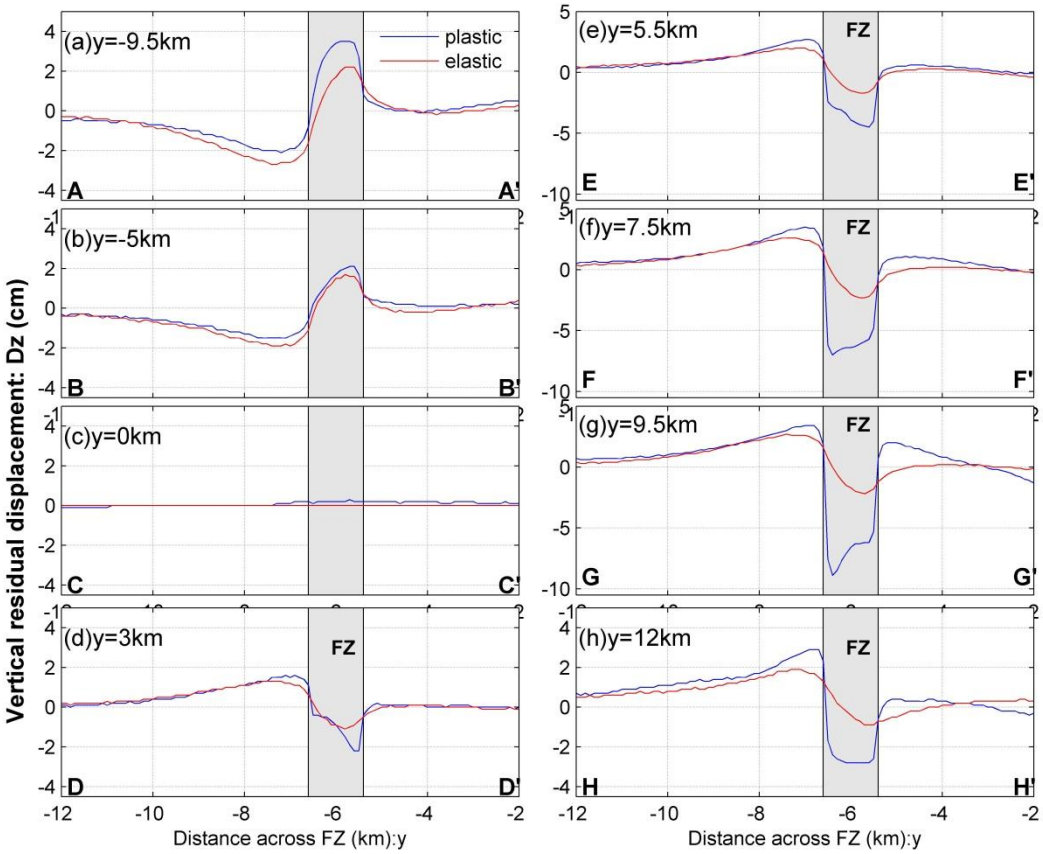

Figure 4. 23 Vertical residual displacements along 8 profiles (locations in Figure 4.21). The blue curves are profiles from the plastic model in Figure 4.21. The red curves are profiles from the elastic model for comparison. Shaded bands correspond to the width of the fault zone.

In this study, experiments are conducted to explore the complete range of plastic parameter (i.e., internal friction coefficient tanφ and cohesion c) choices which allow plastic yielding to occur. Generally, smaller values of internal friction tanφ and cohesion c will give a weaker material that is more susceptible to plastic yielding. The angle of internal friction is a mathematical concept invented to enable researchers in geomechanical analyses. It is a material property that is controlled by a number of

factors, including grain size, grain shape (angularity), relative density, overburden, etc. [Handin, 1969]. We assume smaller values of internal friction and cohesion based on the nature of compliant fault zone is a material with intense fracturing, grain boundary sliding and brecciation. However, we remark that a more accurate fault zone estimations still require constrains on rock material properties (i.e., tanφ and c) from the rock mechanic experiments in the lab.

Previous study of Duan et al [2011] on inelastic response of fault zone to the nearby earthquake pointed out that for better fault zone estimations, one need to take into consideration of both the inelastic and elastic deformation. Our previous 2D studies are on a horizontal plane, which is missing the displacement component in the vertical direction. Thus, some deductions and conclusions may not be straightforward. However, results from elastic models in this study suggest that fault zone width effect on the vertical residual displacement field is more complex than a linear trend as suggested in previous InSAR studies.

We remark that this study does not attempt to compare with data, since the latter requires more realistic fault geometry, accurate regional stress field and constrains from the final slip distribution on rupture fault. That will be part of the future work.

4.5 Conclusion

Compliant fault zone responses to the nearby dynamic ruptures are examined in this study by considering a 3D right-lateral rupture fault associated with a nearby pre-existing fault zone in both elastic and elastoplastic inhomogeneous media. Plastic strain is found along the entire fault zone near the Earth's surface and in the extensional

quadrant at depth when initial stress is close to failure. Plastic parameters are explored in detail to test the complete range that allows plastic strain to occur. Generally, smaller values of internal friction tanφ and cohesion c will give a weaker material that is more susceptible to plastic yielding. If plastic strain does occur, whether it is strong enough to make a sympathetic motion in the fault-parallel residual displacement component, or it is weaker and only gives rise to a reduced retrograde motion of residual displacement in the fault-parallel direction, it is possible to distinguish inelastic response from the elastic one. Once we identify the inelastic deformation, it may further provide some constrains to the absolute stress levels within fault zones, since plastic deformation only occurs when the initial stress is close to failure. Fault zone models with various geometries (i.e., different fault zone depth, width and shape) and rigidity reduction properties are also conducted in this study. Our results suggest that residual displacement increases with fault zone depth and rigidity reduction, however the fault zone width effect does not exhibit a linear relationship. Instead, for fault zone width effect, there is a difference between the deeper fault zone and the shallower fault zone. The fault zone shape may introduce some trade-offs with other fault zone geometry factors (e.g., fault zone depth, width and rigidity reduction property). The presence of plastic strain, especially the extensive one occurring in the extensional quadrant at depth, enhances the residual displacement and further complicates the fault zone geometry effect on the displacement field. All the above mentioned factors need to be taken into account for better fault zone estimations.

CHAPTER V

ELASTIC AND INELASTIC RESPONSES OF THE CALICO AND RODMAN FAULT ZONES TO THE 1992 LANDERS EARTHQUAKE

The studies in the previous two chapters are both from the theoretical point of view to explore the fault zone response to the nearby rupture. However, this dissertation study is not solely speculative. It is motivated by both the observation of Vidale and Li [2003] that Johnson Valley Fault segment may respond to the nearby earthquake plastically (see Introduction chapter for details) and the mismatch between the InSAR observation and the elastic inhomogeneous model prediction that we noticed in literatures [e.g., Cochran et al., 2009; Barbot et al., 2009]. The dynamic simulation results show that some portions of fault zone (i.e. some portion of the extensional quadrant at depth and both the extensional and compressional quadrants near the Earth's surface) experience inelastic deformation, while the remaining portion of fault zone responds to dynamic rupture elastically. Both the finding of Vidale and Li [2003] and our simulation results show the concurrency of elastic and inelastic deformation of fault zone to the nearby rupture. They suggest that taking into account of the inelastic deformation would make the estimation of small-scaled surface displacement more accurate.

In this chapter, I extend the theoretical simulation in an idealized planar rupture fault system into one in a realistically complex fault system in the East California Shear Zone (ECSZ). I compare our simulation results with the geodetic observations to provide an alternative explanation of these observations and a better fit by our elastoplastic models.

5.1 Study Area and Regional Geology

The East California Shear Zone (ECSZ) is a region of active deformation that strikes northwest-southeast across the central Mojave Desert [Sauber et al. 1994]. Active deformation within the ECSZ was highlighted by the occurrence of the 1992 Mw 7.3 Landers and the 1999 Mw 7.1 Hector Mine earthquake. There are primarily three segments of Landers rupture fault. They are Johnson Valley fault (JVF), Emerson fault (EM) and Camp Rock fault (CRF), from southeast to northwest, respectively. The azimuth of the three segments is 350°, 332° and 316°, from southeast to northwest respectively [Hauksson, 1994; Aochi and Fukuyama, 2002]. We simplify the Landers fault system with only these three fault segments while ignore the overlaps and sub-fault between them (Figure 5.1). Also, we modify the azimuth of CRF segment into 314°, for 3D meshing purpose. In addition, Figure 5.1 shows the compliant fault zones examined in this study: Calico fault zone and Rodman fault zone. The distance between Emerson fault segment and Calico fault zone is ~ 10 km, while the distance between the center of Calico and Rodman fault zone is ~5 km.

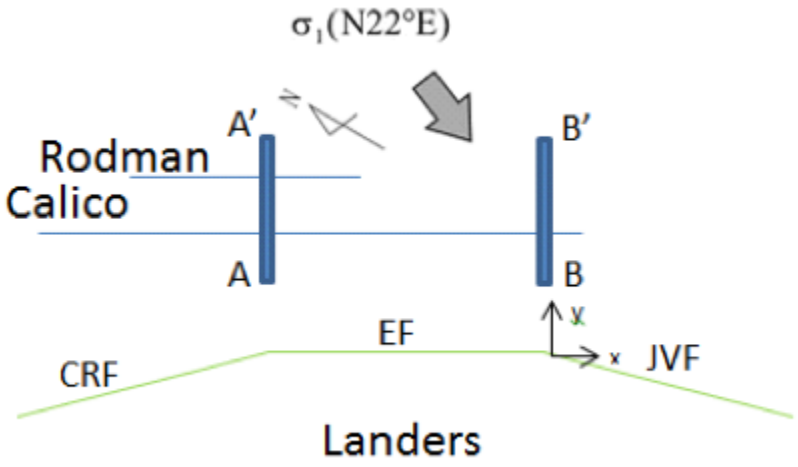

Figure 5. 1 Landers fault traces (in green color) and the nearby compliant fault zones. Profiles AA' and BB' will be explored in details in Figure 5.6, 5.8 and 5.9. The origin of coordinate system is on the interception of the Emerson and Johnson Valley fault segments.

The InSAR LOS (Line Of Sight) displacements induced by the 1992 Landers earthquake are the major data we need for this research. These data have been reported in previous InSAR studies [Fialko, 2002; Barbot et al., 2009; Cochran et al., 2009]. The regional stress field is reported in the Mojave Desert [e.g., Hauksson, 1994] to be N22°E (Figure 5.1), which we use as the uniform stress over the whole working region.

5.2 Rupture Process and Final Slip Distribution on the Ruptured Faults

The landers fault rupture process and the final slip distribution on the faults play an important role in its dynamic stress perturbation and determine the small-scale displacement field of the nearby fault zone, especially in the regard of the fault zone inelastic response. In our simulations, we use the heterogeneity of the static and dynamic frictional coefficient in the slip weakening friction law, to control the rupture process

and the final slip distribution on the faults that are revealed by kinematic inversions [Wald and Heaton, 1994].

Figure 5.2 shows the final slip distribution on the Landers faults from our numerical simulation. As shown in figures 5.2, the hypocenter of the Landers earthquake is at the Johnson Valley fault segment (right hand side), at depth around 7.5 km. The Landers rupture only propagates ~10 km down of Southeast direction; however, it travels along Northwest direction and jumps over further to the Emerson fault segment, and latter Camp rock fault segment. Overall, Landers rupture travels ~78 km along strike, 15 km along depth. The largest final slip is on the west of Emerson fault segment and at the magnitude of ~6 m. For Camp Rock fault segment, final slip is concentrate on the upper right part of fault segment and the largest final slip is at the magnitude of 5 m. Notice that the Johnson Valley fault segment is where the rupture initiated, but the final slip is relatively small in magnitude. Bouchon et al [1998] reported that previous events had already made the Johnson Valley fault very close to failure.

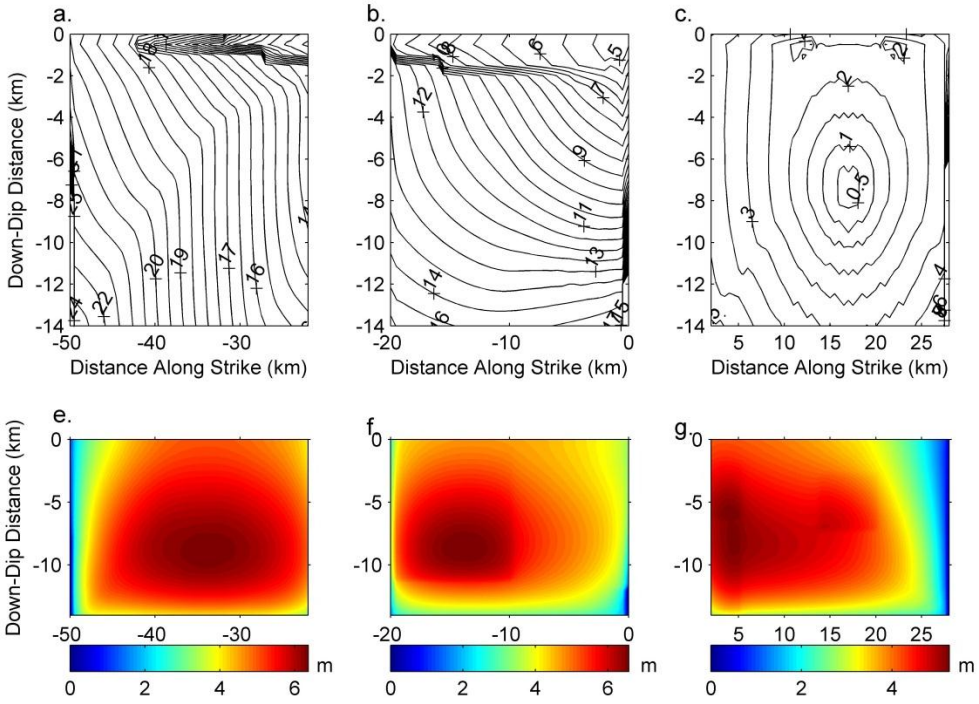

Figure 5. 2 Simulated rupture contours (a, b, c) and the final strike-slip (e, f, g) on Camp Rock, Emersion, Johnson Valley fault segment, respectively. Contour interval is 0.5 s.

The magnitude of final slip on fault is determined by the amount of coseismic stress drop on the faults; While the dynamic rupture speed is determined by a quantity called seismic S value, which is a measure of how near the initial stress field is to failure (see Day, 1982 for definition of S). The larger the S value is, the slower the dynamic rupture travels. Given the initial stress condition constrained by Hauksson [1994]'s observations, we test the different values of static and dynamic frictional coefficient to make certain amount of stress drop and proper S value in order to get the dynamic rupture process close to kinematic inversions [Wald and Heaton, 1994].

5.3 The Surface Displacement Field from the Landers Dynamic Rupture Simulation and Comparison with InSAR Observations in the East California Shear Zone

The Landers dynamic rupture simulations in this chapter using finite element size of 500 m along x and z direction in the main working region; While the grid size is 162.5 m in y direction with our 3D meshing scheme. Simulations are terminated at 40 second, at which the slip on the fault reaches the static value.

Similar as in the previous two chapters, two types of models: the target model with compliant fault zones and the reference model which has homogeneous medium are conducted in this study. By subtracting the final displacement of the reference model from that of the target model, we get the residual displacement that gives the effect from the presence of fault zones explicitly. Inelastic response is allowed in this simulation by using Drucker-Prager criterion to calculate the plastic strain accumulated over time steps. The plastic parameters used here are: internal frictional angle, $\tan\varphi=0.58$ and cohesion $c=0.1$ MPa for compliant fault zone material; while $\tan\varphi=0.85$ and $c=20$ MPa for the intact rocks.

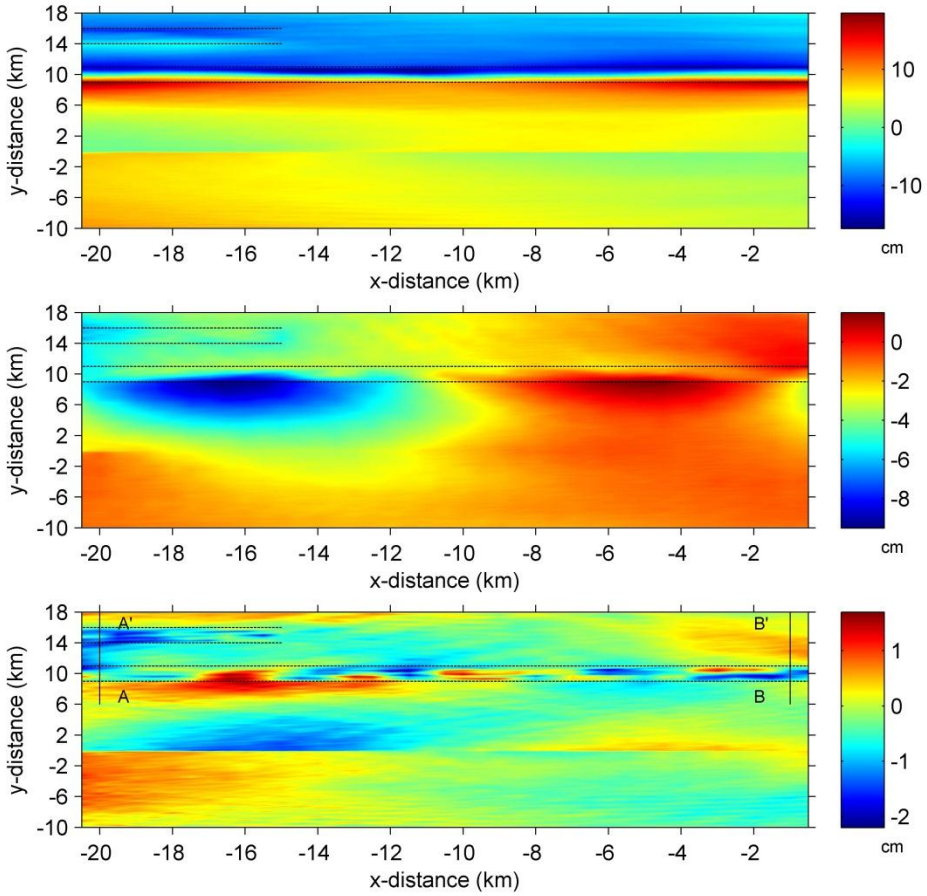

Figure 5. 3 Residual displacements (see Figure 5.4 for definition) on the Earth's surface induced by Landers earthquake in 3D elastoplastic inhomogeneous medium with Calico and Rodman compliant fault zone. (a) fault-parallel (x) component Dx, (b) fault-normal (y) component Dy, (c) vertical (z) component Dz. Black dash lines delimit the fault zone. AA'(x= -20 km) and BB' (x= - 0.5 km) are two profiles shown in Figure 5.4, 5.5 and 5.6.

Figure 5.3 shows the residual displacement field around the Emerson segment of the Landers rupture simulation. Calico and Rodman fault zone are at 10 km and 15 km north above the Emerson rupture segment, respectively. The presence of fault zones clearly

has an impact on the residual displacement field. But the impact is different at each residual displacement component. AA' and BB' are two profiles that across the fault zones, which will be explored in detail in Figure 5.4 to 5.6.

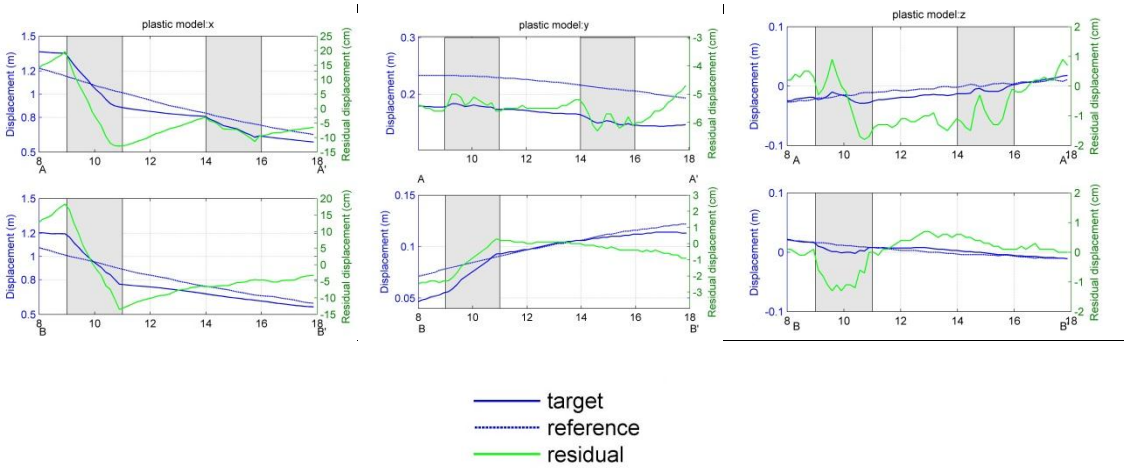

Figure 5. 4 Residual displacements along profile AA' and BB'(see Figure 5.3 for locations). Residual displacement (green curve, in centimeter on the right axis) is calculated by subtracting static displacement (in meter on the left axis) of a reference model (dash blue) from that of the target model (solid blue). Shaded bands correspond to the width of the fault zone.

Figure 5.4 displays the profile views along AA' and BB' of residual displacement along the x, y and z directions, respectively. Profile AA' is across both the Calico and the Rodman fault zones; While profile BB' is only across the Calico fault zone. The structure of Calico fault zone of 4 km deep, 2 km wide and 40% seismic wave velocity reduction are used in this simulation. All the other parameters are the same for the Rodman fault zone, while the depth of Rodman fault zone is only 2 km.

Interferometric synthetic aperture radar (InSAR) is a radar technique used in geodesy and remote sensing, which can measure centimeter-scale deformation changes over spans of days to years. This technique has been widely used in earthquake study. Satellite orbits around the Earth surface, sending signals with certain wavelength to the Earth's surface and receiving the signal reflected back. The reflected signal contains information about the Earth's surface. With the interferometry of the two sets of satellite signal that obtained over the same region but during different times, the specific changes (e.g., from an earthquake event) of the Earth's surface will be recorded by InSAR data. There are two important directional quantities in InSAR data acquisition: the satellite radar incidence angle λ and the azimuth of the satellite heading vector φ (positive clockwise from the north). With the information of λ and φ, one can use equation (3) [Fialko et al, 2001], to synthesize the InSAR Line Of Sight (LOS) displacement. In equation (3), Un, Ue and Uu represents residual displacement along north, east and vertical up directions, respectively.

$$[Un \sin\varphi - Ue \cos\varphi] \sin\lambda + Uu \cos\lambda + \delta_{los} = d_{los} \quad (3)$$

The InSAR studies of 1992 Landers earthquake available in literatures [e.g., Fialko, 2004; Cochran et al, 2009; Barbot et al, 2009] are using ERS-1 data, where the satellite incidence angle λ=23° and the satellite heading vector φ=188.55° for descending orbits.

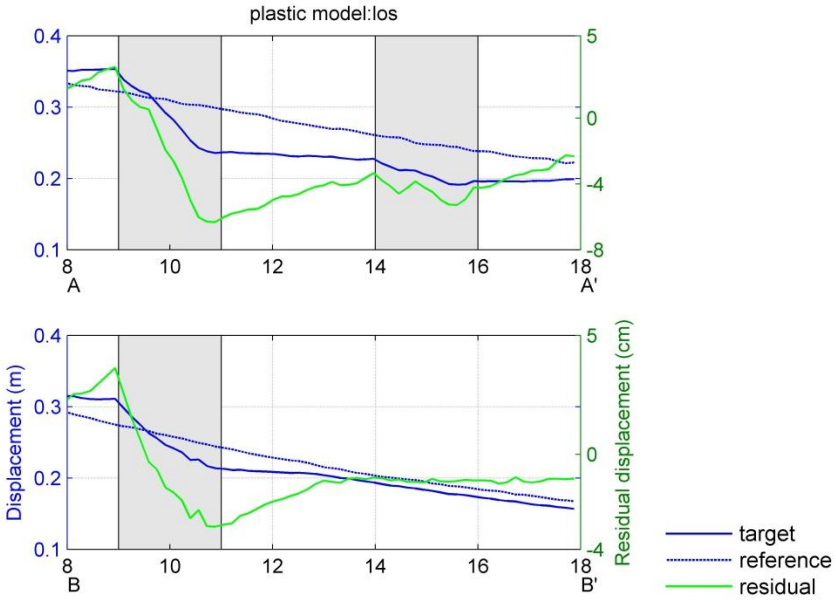

Figure 5. 5 (a) Residual displacements along profile AA' and BB'(see Figure 5.3 for locations) from plastic models, synthetic to InSAR LOS direction. Residual displacement (green curve, in centimeter on the right axis) is calculated by subtracting static displacement (in meter on the left axis) of a reference model (dash blue) from that of the target model (solid blue). Shaded bands correspond to the width of the fault zone.

Using the above directional information, we synthesize InSAR LOS displacements from the results of our dynamic rupture simulation from plastic models as shown in Figure 5.5.

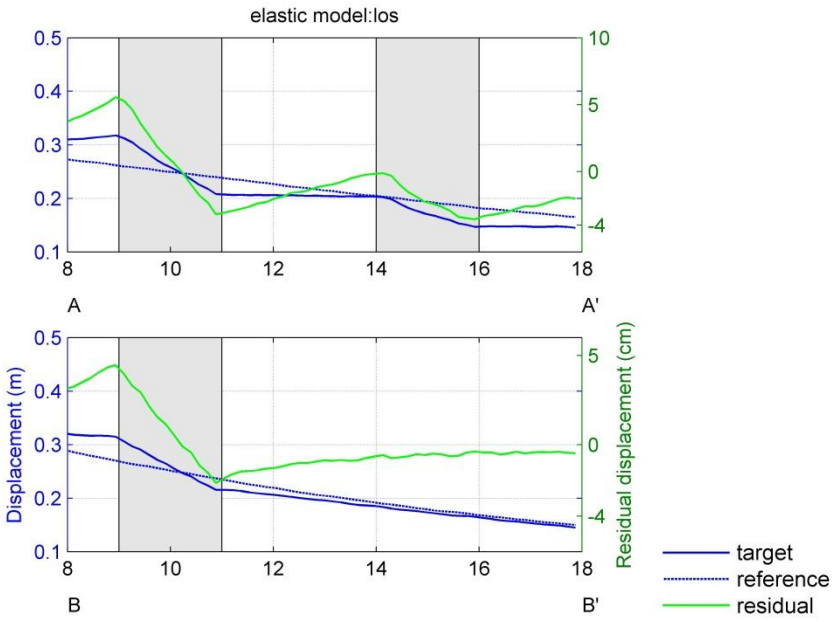

Figure 5. 6 (a) Residual displacements along profile AA' and BB'(see Figure 5.3 for locations) from elastic models, synthetic to InSAR LOS direction. Residual displacement (green curve, in centimeter on the right axis) is calculated by subtracting static displacement (in meter on the left axis) of a reference model (dash blue) from that of the target model (solid blue). Target model and reference model are defined as in Figure 3.1 (a) and (b), respectively. Shaded bands correspond to the width of the fault zone.

To illustrate the effects of inelastic response of the compliant fault zone on the displacement field, we also run another pair of a target model and a reference model. The only change in this pair of models, with respect to the above pair of models, is that a much higher value of cohesion (e.g., 10000 MPa) is assigned to the entire model region so that no off-fault yielding will occur in this pair of models. We refer this pair of models as the elastic models. We also get the residual displacement from the elastic models and further synthesize it into the InSAR LOS direction, as shown in Figure 5.6.

Although all the other parameters, including the rupture process and compliant fault zone geometry and rigidity reduction properties, are the same as in the plastic model, the LOS displacements from plastic and elastic model show differences. The most striking one is the subsidence occurring across Calico fault zone along profile AA' from plastic model in Figure 5.5 is ~6 cm; while that from elastic model is ~4 cm. Compared the profile view of LOS displacement along AA' from the InSAR observation (e.g., Barbot el al, [2009], Figure 6a), our synthesized LOS displacement along AA' from plastic models in Figure 5.5 match the magnitude of the LOS displacement observation better. This suggests the importance to take into account of the inelastic response to understand the fault zone responses to the nearby rupture.

CHAPTER VI

SUMMARY AND CONCLUSIONS

Inelastic response of a compliant fault zone to nearby earthquakes requires dynamic analyses. Using spontaneous rupture models in a 3D half space, we investigate the distribution of plastic strain within a fault zone and its effects on surface displacement fields around the fault zone. We find that when the fault zone rocks are close to failure in the prestress field, plastic strain occurs along the entire fault zone near the Earth's surface and along some portions of the fault zone in the extensional quadrant at depth, while the remaining part of fault zone deform elastically. Plastic strain within the fault zone enhances the surface vertical displacement of the fault zone, and the enhancement in the extensional quadrant is significantly larger in magnitude than that in the compressive quadrant. The enhancement by inelastic response of the fault zone may be mapped into inaccurate estimates of the fault zone structure and/or properties from observed displacement fields if elastic response is assumed, in particular in the extensional quadrant of an earthquake rupture. By resolving the horizontal and vertical surface displacement from the line-of-sight displacement in InSAR images, one can distinguish inelastic response from elastic response of a compliant fault zone. Compared with purely elastic response, inelastic response of a compliant fault zone results in sympathetic motion (or reduced retrograde motion) in the fault-parallel horizontal displacement while enhanced vertical displacement in a strike-slip fault system.

The geometry and properties of compliant fault zone may contain information of past earthquake ruptures and subsequent healing processes. The fault zone structure and properties, including the width, depth, shape of the fault zone, rigidity reduction and the plastic yielding occurring within the fault zone, all have impact on the surface displacement. The different parameter choices may lead to the same residual displacements from different models. Taking into account of all the possible parameter choices, especially the inelastic response of fault zone, may improve our understanding of small-scale deformation signals around pre-existing faults due to nearby earthquakes. Further, it may lead to better estimation of fault zone structures and rigidity reduction property.

Dynamic rupture simulations of Landers earthquake are conducted in both the elastoplastic and purely elastic inhomogeneous media in order to fit the small-scale surface displacement in ECSZ reported in literatures. The results from plastic models fit better to the observation than those from the elastic models, suggesting it is important to take into account inelastic response to for better understanding small-scale surface displacements associated with compliant fault zones.

REFERENCES

Andrews, D. J. (2005), Rupture dynamics with energy loss outside the slip zone, J. Geophys. Res., 110, B01307, doi:10.1029/2004JB003191.

Andrews D. J. (1976), Rupture velocity of plane-strain shear cracks, J. Geophys. Res., 81, 5679–5687.

Aochi, H., and E. Fukuyama (2002), Three-dimensional nonplanar simulation of the 1992 Landers earthquake, J. Geophys. Res., 107, B2, ESE4-1–ESE4-12, doi:10.1029/2000JB000061.

Barbot, S., Y. Fialko, and D. Sandwell (2009), Three-dimensional models of elasto-static deformation in heterogeneous media, with applications to the Eastern California Shear Zone, Geophys. J. Int., 179, 500–520.

Ben-Zion, Y. and C. G. Sammis (2003), Characterization of Fault Zones, Pure Appl. Geophys., 160, 677-715.

Bouchon, M., M. Campillo, and F. Cotton (1998), Stress field associated with the rupture of the 1992 Landers, California, earthquake and its implications concerning the fault strength at the onset of the earthquake, J. Geophys. Res., 103, 21091–21097.

Chester, F. M. and J. S. Chester (1998), Ultracataclasite structure and friction processes of the Punchbowl fault, San Andreas system, California, Tectonophysics, 295, 199-221.

Chester, F. M., J. P. Evans, and R. L. Biegel (1993), Internal structure and weakening mechanisms of the San Andreas Fault, J. Geophys. Res., 98, 771–786.

Cochran, E.S., Y.-G. Li, P.M. Shearer, S. Barbot, Y. Fialko, and J.E. Vidale (2009), Seismic and geodetic evidence for extensive, long-lived fault damage zones, Geology, 37, 315-318.

Day S. M (1982), Three Dimensional simulation of spontaneous rupture: the effect of nonuniform prestress, Bull. seism. Soc. Am, 72, 1881-1902.

Drucker, D. C. and W. Prager (1952), Soil mechanics and plastic analysis or limit design, Q. Appl. Math., 10, 157–165.

Duan, B. (2010a), Inelastic response of compliant fault zones to nearby earthquakes, Geophys. Res. lett., L16303, doi:10.1029/2010GL044150.

Duan, B. (2010b), Role of initial stress rotations in rupture dynamics and ground motion: A case study with implications for the Wenchuan earthquake, J. Geophys. Res., 115, B05301, doi:10.1029/2009JB006750.

Duan, B. (2008a), Effects of low-velocity fault zones on dynamic ruptures with nonelastic off-fault response, Geophys. Res. Lett., 35, L04307, doi:10.1029/2008GL033171.

Duan, B. (2008b), Asymmetric off-fault damage generated by bilateral ruptures along a bimaterial interface, Geophys. Res. Lett., 35, L14306, doi:10.1029/2008GL034797.

Duan, B., and S. M. Day (2008), Inelastic strain distribution and seismic radiation from rupture of a fault kink, J. Geophys. Res., 113, B12311, doi:10.1029/2008JB005847.

Duan, B., and D. D. Oglesby (2006), Heterogeneous fault stresses from previous earthquakes and the effect on dynamics of parallel strike-slip faults, J. Geophys. Res., 111, B05309, doi:10.1029/2005JB004138.

Duan, B., J. Kang, and Y.-G. Li (2011), Deformation of compliant fault zones induced by nearby earthquakes: Theoretical investigations in two dimensions, J. Geophys. Res., 116, B03307, doi:10.1029/2010JB007826.

Ellsworth, W. L. and P. E. Malin (2006), A first observation of fault guided PSV-waves a SAFOD and its implications for fault characteristics, EOS Trans. AGU, 87(52), Abstract T23E-02.

Fialko, Y. (2004), Probing the mechanical properties of seismically active crust with space geodesy: Study of the coseismic deformation due to the 1992 Mw 7.3 Landers (southern California) earthquake, J. Geophys. Res., 109, B03307, doi:10.1029/2003JB002756.

Fialko, Y., D. Sandwell, D. Agnew, M. Simons, P. Shearer, and B. Minster (2002), Deformation on nearby faults induced by the 1999 Hector Mine earthquake, Science, 297, 1858-1862.

Fialko, Y., M. Simons, and D. Agnew (2001), The complete (3-D) surface displacement field in the epicentral area of the 1999 Mw7.1 Hector Mine earthquake, California, from space geodetic observations, Geophys. Res. Lett., 28, 3063-3066

Handin, J. (1969), On the Coulomb-Mohr failure criterion, J. Geophys. Res. 74, 5343–5348.

Hauksson, E. (1994), State of stress from focal mechanisms before and after the 1992 Landers earthquake sequence, Bull. Seismol. Soc. Am., 84, 917–934

Harris, R. A., M. Barall, D. J. Andrews, B. Duan, S. Ma, E. M. Dunham, A. -A. Gabriel, Y. kaneko, Y. Kase, B. T. Aagaard, D. D. Oglesby, J. -P. Ampuero, T. C. Hanks, and N. Abrahamson (2011), Verifying a computational method for predicting extreme ground motion, Seism. Res. Lett., 82, 5, 638-644, doi:10.1785/gssrl.85.5.638.

Harris, R. A., M. Barall, R. Archuleta,E. Dunham, B. Aagaard, J. P. Ampuero, H. Bhat, V. Cruz-Atienza, L. Dalguer, P. Dawson, S. Day, B. Duan, G. Ely, Y. Kaneko, Y. Kase, N. Lapusta, Y. Liu, S. Ma, D. Oglesby, K. Olsen, A. Pitarka, S. Song, and E. Templeton (2009), The SCEC/USGS dynamic earthquake-rupture code verification exercise, Seismol. Res. Lett., 80, 1, 119-126, doi:10.1785/gssrl.80.1.119.

Hearn, E. and Y. Fialko (2009), Can compliant fault zones be used to measure absolute stresses in the upper crust? J. Geophys Res., 114, B04403, doi:10.1029/2008JB005901

Ida, Y. *(*1972*),* Cohesive force across the tip of a longitudinal-shear crack and Griffith's specific surface energy, J. Geophys. Res., 77, 20, 3796–3805, doi*:*10.1029/JB077i020p03796*.*

Jaeger, J. C., and N. G. W. Cook (1976), Fundamentals of Rock Mechanics, Chapman and Hall, London.

Kang, J. and Duan, B. (2014), Inelastic response of compliant fault zones to nearby earthquakes in three dimensions, Tectonophysics., 612–613, 56–62, doi: 10.1016/j.tecto.2013.11.033.

Kramer, S. L. (1996), Geotechnical Earthquake Engineering, Prentice Hall, Upper Saddle River, N. J.

Li, Y.-G., *and* P. E. Malin (2008), San Andreas Fault damage at SAFOD viewed with fault-guided waves, Geophys. Res. Lett., 35, L08304, doi:10.1029/2007GL032924.

Li, Y.-G., Chen, P., Cochran, E.S., Vidale, J.E., and Burdette, T., (2006), Seismic evidence for rock damage and healing on the San Andreas Fault associated with the 2004 M 6.0 Parkfield earthquake: Seismological Society of America Bulletin, 96, S349–S363, doi: 10.1785/0120050803.

Li, Y.-G., J. E. Vidale, K. Aki, D. Xu, T. Buedette (1998), Evident of shallow fault zone strengthening after the 1992 M7.5 Landers, California, earthquake, Science, 279, 217-219, doi:10.1126/science.279.5348.217.

Lockner, D. A., D. E. Moore, Z. Reches (1992), Microcrack interaction leading to shear fracture, Proc. 33rd U.S. Symp. Rock Mech., 807–816.

Ma, S. (2008), A physical model for widespread near-surface and fault zone damage induced by earthquakes, Geochem. Geophys. Geosyst., 9, Q11009, doi:10.1029/2008GC002231.

Ma, S., and D. J. Andrews (2010), Inelastic off-fault response and three-dimensional dynamics of earthquake rupture on a strike-slip fault, J. Geophys. Res., 115, B04304, doi: 10.1029/2009JB006382.

Sauber, J., Tatcher, W., Solomon, S.C. & Lisowski, M. (1994), Geodetic slip rate for the east California shear zone and the recurrence time of Mojave desert earthquakes, Nature, 367, 264–266.

Scholz, C. H., N. H. Dawers, J.-Z. Yu, M. H. Anders, and P. A. Cowie (1993), Fault Growth and Fault Scaling Laws: Preliminary Results, J. Geophys. Res., 98, B12, 21951–21961, doi: 10.1029/93JB01008.

Templeton, E. L., and J. R. Rice (2008), Off-fault plasticity and earthquake rupture dynamics, 1. Dry materials or neglect of fluid pressure changes, J. Geophys. Res., 113, B09306, doi: 10.1029/2007JB005529.

Vidale, J. and Y.-G. Li (2003), Damage to the shallow Landers fault from the nearby Hector Mine earthquake, Nature, 421, 524-526.

Wald, D. J., and T. H. Heaton (1994), Spatial and temporal distribution of slip for the 1992 Landers, California, earthquake, Bull. Seismol. Soc. Am., 84, 668– 691.

Wu, X., B. Duan , and V. Taylor (2011), Parallel simulations of dynamic earthquake rupture along geometrically complex faults on CMP systems, J. Algorithm and Computational Technology, 5, 2, 313-340.

Yang, H., Zhu, L. and Cochran, E. S. (2011), Seismic structures of the Calico fault zone inferred from local earthquake travel time modelling. Geophysical Journal International, 186, 760–770, doi: 10.1111/j.1365-246X.2011.05055.x